Impact of wildfire smoke on Arctic cirrus formation, part 2: simulation of MOSAiC 2019-2020 cases

Albert Ansmann[1], Cristofer Jimenez[1], Daniel A. Knopf[2], Johanna Roschke[1], Johannes Bühl[1,3], Kevin Ohneiser[1], and Ronny Engelmann[1]

[1]Leibniz Institute for Tropospheric Research, Leipzig, Germany
[2]School of Marine and Atmospheric Sciences, Stony Brook University, Stony Brook, NY 11794, USA
[3]Harz University of Applied Sciences, Wernigerode, Germany

Correspondence: A. Ansmann
(albert@tropos.de)

Abstract.

A simulation study of the potential impact of wildfire smoke on Arctic cirrus formation is presented. The simulations complement the MOSAiC (Multidisciplinary drifting Observatory for the Study of Arctic Climate) field observations, discussed in part 1. The observations suggest that Siberian wildfire smoke had a strong impact on Arctic cirrus formation in the winter of 2019-2020. Via simulations, a detailed insight into the potential of wildfire smoke to influence Arctic cirrus formation as a function of observed meteorological and environmental conditions (temperature, relative humidity, large-scale and gravity-wave-induced lofting conditions, ice-nucleating particle (INP) concentration) is provided. Lidar-derived values of the INP concentration (INPC) serve as input and ice crystal number concentration (ICNC) values retrieved from combined lidar-radar observations are used for comparison with the simulation results. The simulations show that the observed smoke pollution levels in the upper troposphere were high enough to trigger strong ice nucleation. The simulations also corroborate the hypothesis, stated in part 1, that the persistent smoke layer, continuously observed over the central Arctic during the winter half year 2019-2020, was able to widely suppress homogeneous freezing so that the smoke aerosol most probably controlled cirrus formation and properties. The observations suggest that the INP reservoir was continuously refilled from the lower stratosphere. Furthermore, the simulations confirm that the observed high ice saturation ratios of 1.3–1.5 over the North Pole region at cirrus tops (with top temperatures of -60 to -75°C) point to inefficient INPs as expected when wildfire smoke particles (organic particles) serve as INPs. Finally, the simulations revealed that ice nucleation in wide spread and frequently occurring shallow updrafts (with low amplitudes) seem to be responsible for the observed low ICNC values of typically 1-50 L^{-1} in the Arctic cirrus virga.

1 Introduction

The MOSAiC (Multidisciplinary drifting Observatory for the Study of Arctic Climate) expedition (Shupe et al., 2022) offered the unique opportunity to investigate the **potential** impact of wildfire smoke on cirrus formation. During the one year MOSAiC field campaign from October 2019 to September 2020, aged Siberian wildfire smoke **in the upper troposphere and lower**

stratosphere (UTLS) covered the central Arctic during the first 7.5 months (October 2019 to mid-May 2020) (Ohneiser et al., 2021; Ansmann et al., 2024). Ice clouds frequently developed in the smoke-polluted upper tropospheric air masses.

In part 1 (Ansmann et al., 2025), we presented **our MOSAiC observations of smoke and cirrus properties during the winter half year 2019-2020.** Lidar and radar measurements were performed aboard the research ice breaker *Polarstern* which drifted with the pack ice in the North Pole region. **The MOSAiC observations provided strong indications that the permanently observed upper tropospheric wildfire smoke layer (consisting of organic aerosol particles) controlled cirrus formation during the entire winter half year and widely suppressed homogeneous freezing of background aerosol particles. Furthermore, high ice saturation ratios of 1.3-1.5, often found in the radiosonde data in the upper part of the extended cirrus fields, point to heterogeneous ice nucleation on inefficient ice-nucleating particles (INPs) as expected when organic particles serve as INPs (Kanji et al., 2008; Wang and Knopf, 2011; Knopf et al., 2018).**

The simulations in this part 2 complement the MOSAiC field observations in part 1. Models enable us to better understand the complex processes of ice nucleation, ice growth, and sedimentation at given temperature, humidity and large-scale and gravity-wave-related lofting conditions. The most important questions to be answered in this part 2 are: 1) Can the ice crystal number concentrations (ICNCs) observed in Arctic cirrus clouds (see part 1), be reproduced by simulations of heterogeneous ice nucleation on organic particles by using the measured smoke pollution levels as input in the simulations? 2) How large was the contribution of homogeneous freezing of background aerosol particles to the observed cirrus formation processes?

The paper is organized as follows: In Sect. 2, the simulation model is explained. In Sect 3, we summarize key observational findings, presented in part 1 (Ansmann et al., 2025). The measured virga ICNCs served as a guide in the development of our simulation strategy and were used as orientation in the design of most realistic simulation scenarios. In Sect. 4, we present and discuss the simulation results and provide answers to the two questions stated above. A summary of the main simulation results and conclusions on smoke-cirrus interaction, based on both observations and simulations, are provided in Sect. 5.

2 Simulation model

The model permits the simulation of ice nucleation and growth of ice crystals in an adiabatically ascending air parcel. This air parcel starts in the coldest region of a cirrus layer, i.e., at cloud top, where ice nucleation usually begins. The main steps of the simulations are shown in Fig. 1. All essential atmospheric and aerosol input parameters and values required in the simulations are given in Table 1. The meteorological input data (air pressure p, temperature T, relative humidity RH over water, and corresponding water vapor mixing ratio MR at height z_0) were taken from the MOSAiC radiosonde data base (Maturilli et al., 2022). Typical cirrus top observations are considered. While the November and December ice clouds showed cloud top temperatures of $-60°$ to $-65°$C and cloud top heights were around 9 km, the January and February ice clouds had top temperatures of -70 to $-75°$C and the cirrus top heights were typically above 10 km. We concentrate on the January cirrus scenarios in our simulation study. Examples of January cirrus observations are shown in part 1 (Ansmann et al., 2025) and in Sect 3 of this part 2. The smoke aerosol input data (e.g.,

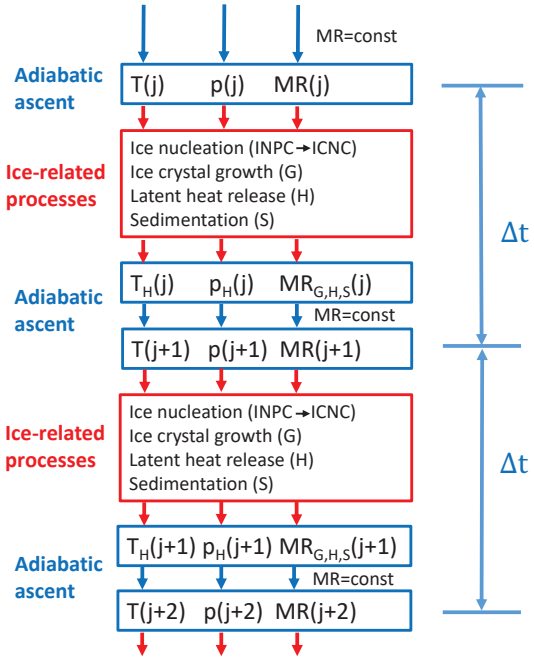

Figure 1. Overview of the simulation steps. An adiabatically ascending, smoke-filled air parcel is simulated. Meteorological input parameters are the air temperature T, air pressure p, relative humidity RH, and water vapor mixing ratio MR at the starting height z_0. The computation of the adiabatic rise of the air parcel is indicated by blue arrows and boxes. Red boxes contain the computation of ice-related processes, i.e., nucleation of ice crystals, growth of ice crystals, heat release, and sedimentation of crystals. These processes influence the meteorological conditions. Indices G, H, and S indicate an impact of ice crystal growth, heat release, and sedimentation on the different meteorological parameters. The vertical (range) resolution is defined by the product of the selected vertical velocity and the temporal resolution Δt in the computation. Computations performed in steps j, $j+1$, and $j+2$ are considered in the sketch.

the particle surface area concentration PSAC, denoted as s_p in equations) were available from lidar observations before and after cirrus events (Ansmann et al., 2025).

The simulation of an ascending smoke-filled air parcel starts at height z_0. Atmospheric input values at z_0 are temperature, pressure, and relative humidity. The smoke PSAC input value is set to a typical value of 10 μm^2 cm^{-3} (required in heterogeneous ice nucleation calculations) and the background volume concentration is set to 1 μm^3 cm^{-3} (required in homogeneous ice nucleation calculations). The air parcel is ascending adiabatically (blue arrows and boxes in Fig. 1) so that temperature T decreases with 0.00984 K m^{-1}. The decrease of air pressure p is obtained by applying the barometric formula. The vertical ascent of an air parcel can be caused by large-scale lofting events (e.g., orographic or frontal lofting events) (Kärcher and Lohmann, 2002) or short-term lofting events, e.g., resulting from gravity wave activity (Haag and Kärcher, 2004; Spichtinger et al., 2005; Podglajen et al., 2016; Kärcher and Podglajen, 2019; Kärcher et al.,

Table 1. Meteorological and aerosol input in the ice nucleation simulations.

Smoke particle surface area concentration	s_{p}	10 μm^2 cm^{-3}
Particle volume concentration, background	$v_{\mathrm{p,bg}}$	1.0 μm^3 cm^{-3}
Reservoir of potential INPs	n_{250}	2000 L^{-1}
Contact angle	c_{angle}	24.5°, 26.5°
Starting height (in ascent simulations)	z_0	9.0 km, 10.5 km
Temperature at z_0	T	213 K, 199 K
Relative humidity over water at z_0	RH	69.5% , 64%
Ice saturation ratio at z_0	S_{i}	1.2
Air pressure at z_0	p	265 hPa, 212 hPa
Updraft mean vertical velocity	v_{up}	0.01-0.2 m s^{-1}
Water vapor deposition coefficient	α_{i}	0.5
Temporal resolution	Δt	0.01–1 s

2019). Updraft speeds are typically in the range of 1-5 cm s^{-1} in the case of large-scale lofting events and 10-30 cm s^{-1} during gravity-wave-induced updraft events.

During the adiabatic rise, the water vapor mixing ratio MR in the air parcel remains constant so that the relative humidity and the respective ice saturation ratio S_{i} increases. After exceeding the ice nucleation onset ice saturation ratio $S_{\mathrm{i,on}}$ strong ice nucleation sets in. The nucleated ice particles start to grow by deposition of water vapor on the crystal surfaces. Ice growth leads to a reduction of water vapor in the air parcel and thus to a decrease of S_{i}. The burst-like ice nucleation event stops when the ice saturation ratio reaches again the onset value and further decreases. The growing ice crystals form a broad size spectrum and, consequently, a broad spectrum of falling velocities develop. A certain amount of the larger crystals with comparably high sedimentation speed leaves the air parcel (sedimentation effect) and does no longer contribute to the reduction of water vapor within the air parcel by ice growth processes. The processes of ice formation, growth, heat release related to ice production, and sedimentation are highlighted in red boxes in Fig. 1. Each simulations step (j, j+1, ...) includes the computation of the adiabatic ascent of the air parcel within the time interval Δt, the computation of the ice-related processes, and the computation of their impact on the meteorological parameters temperature, pressure, and water-vapor mixing ratio. The vertical (range) resolution in the computations is defined by the product of the selected vertical velocity and the temporal resolution Δt. Temporal resolutions down to 0.01 s can be selected in the computations.

Besides heterogeneous nucleation of ice crystals on the smoke INPs (organic particles), homogeneous freezing of the omnipresent liquid sulfate particles is simulated. The main simulation results are time series of number concentrations of heterogeneously and homogeneously nucleated ice crystals, $n_{\mathrm{i,het}}$ and $n_{\mathrm{i,hom}}$, and the total amounts of nucleated ice crystals, $\sum n_{\mathrm{i,het}}$ and $\sum n_{\mathrm{i,hom}}$, nucleated during a simulated updraft event. We widely follow the modeling concept

as given in recent articles of Kärcher et al. (2022, 2023) and Spichtinger et al. (2023). These papers provide a good introduction into state-of-the-art cirrus modeling.

In the following subsections, we describe the different parts of the simulation model. The ice nucleation parameterizations are given Sect. 2.1. The computation of ice crystal growth by deposition of water vapor on the crystals is described in Sect. 2.2. A simple approach to roughly consider sedimentation of ice crystals is outlined in Sect. 2.3.

2.1 Ice crystal nucleation

An accurate analysis of the INP budget requires a prognostic treatment of INPs (Knopf et al., 2023a). Diagnostic and prognostic approaches to ice nucleation parameterization are available, including time-independent (singular) number and surface-area-based descriptions and a time-dependent description following classical nucleation theory (CNT). The choice of the ice nucleation parameterization defines the size of the INP reservoir. Following the singular hypothesis, only a small fraction of the particles (smoke particles in our case) can serve as INPs that are activatable. Following the CNT scheme, by contrast, all smoke particles can be activated on a random base. The introduction of an INP reservoir is the most realistic approach, especially in view of the unlimited amount of available INPs over the North Pole region during the winter 2019-2020.

In our specific approach, INP number concentration (INPC) and ICNC are treated in a prognostic fashion. The transfer from the INPC to ICNC is the first process listed in the red boxed in Fig. 1. This means we account for sources and sinks of INPs and ice crystals as discussed in detail by Knopf et al. (2023a). The smoke particles are considered as the source of INPs. Once the INPs activate and form ice crystals, these INPs are removed from the INP reservoir (sink of INPs). The source of ice crystals are the activated INPs. To account for the time-dependence of ice nucleation, ice crystal growth and removal processes, taking place simultaneously, we chose an ice nucleation parameterization based on CNT (Knopf and Alpert, 2023). In CNT, the heterogeneous ice nucleation rate coefficient, $J_{\rm het}$ in units of cm^{-2} s^{-1}, describes the number of ice nucleation events per particle surface area and time. Multiplication with particle surface area yields an ice nucleation rate in units of s^{-1}, ultimately determining the number of ice nucleation events, i.e., ice crystal number concentration per modeling time step. Another feature of our model is that we assume that the INP reservoir consists of all available smoke particles with radius >250 nm. This means that all smoke particles of the large-particle fraction (n_{250}) are potentially activatable INPs in an air parcel. Here, we follow the argumentation given in Knopf et al. (2023a). **Because of the specific smoke conditions during the MOSAiC winter half year with an unlimited downward flux of smoke particles from the stratosphere, we could even set the INP reservoir to 'unlimited'.**

We selected temporal resolutions from 0.1 to 1 s in the simulations for updraft scenarios with vertical velocities from 20 cm s^{-1} to 1 cm s^{-1}. We found that a temporal resolution Δt of 1, 0.5, and 0.1 s is sufficient to adequately resolve the burst-like ice nucleation events in air parcels ascending with a vertical velocity of 1, 3, and 20 cm s^{-1}, respectively.

Regarding heterogeneous nucleation of ice crystals on organic aerosol particles at cirrus temperatures we apply the deposition ice nucleation (DIN) parameterization (Wang and Knopf, 2011). The method is also outlined in Ansmann et al. (2021) for

lidar applications. The predicted number concentration of ice crystals (ICNC, in cm^{-3}) is given by

$$n_{\mathrm{i,het}} = s_{\mathrm{p}} \times J_{\mathrm{het}}(c_{\mathrm{angle}}, T, S_{\mathrm{i}}) \times \Delta t \quad (1)$$

with the smoke particle surface area concentration s_{p} (in cm^{-2} cm^{-3}), also denoted as PSAC, and the nucleation time interval Δt (in s). The retrieval of s_{p} from lidar backscatter observations is described in Ansmann et al. (2021, 2023). The nucleation rate coefficient J_{het} is a function of the contact angle c_{angle}, ice nucleation temperature T and ice saturation ratio S_{i}, i.e., the ratio of the partial pressure of water vapor p_{w} and saturation vapor pressure with respect to ice $p_{\mathrm{i,sat}}$. The contact angles for organic aerosol are in the range of 22°-30° (Wang and Knopf, 2011). With increasing ice-nucleation efficiency the contact angle decreases. For mineral dust, the contact angle is in the range of 10°-15° (Wang and Knopf, 2011). In the model, the contact angle increases with temperature. The respective ice nucleation onset value $S_{\mathrm{i,on}}$ is about 1.25-1.3 for a contact angle of 23.5° at 220 K and 1.45-1.5 for a contact angle of 26.5° at 200 K (Wang and Knopf, 2011; Wang et al., 2012). Regarding the organic material, leonardite (a standard humic acid surrogate material) is assumed to represent the amorphous organic coating of smoke particles. Leonardite, an oxidation product of lignite, is a humic-acid-containing soft waxy particle (mineraloid), black or brown in color, and soluble in alkaline solutions. The INP characteristics of leonardite were studied in detail in laboratory experiments (Kanji et al., 2008; Wang and Knopf, 2011; Knopf and Alpert, 2013; Rigg et al., 2013).

Eq. (1) assumes that all wildfire smoke particles are potential INPs, thus contributing to the INP reservoir (Knopf et al., 2023a). According to the discussion in Sect. 3.2 in Ansmann et al. (2025), the observed MOSAiC particle surface area concentration s_{p} (or PSAC) was of the order of 10 μm^2 cm^{-3}. In our simulations, we restricted the INP reservoir to the particle number concentration n_{250} (considering particles with radius $>$ 250 nm), assuming that the large particle fraction contains the most favorable INPs (DeMott et al., 2010). n_{250} is about 2000 L^{-1} for s_{p} values of 10 μm^2 cm^{-3}. More details to the INP reservoir are given in Sect. 2.1.1. As mentioned above, once an INP is activated to form an ice crystal, this INP (and the respective contribution to PSAC) is removed from the INP reservoir in the simulation.

We also simulate ice nucleation via homogeneous freezing (Koop et al., 2000; Knopf and Rigg, 2011; Schneider et al., 2021):

$$n_{\mathrm{i,hom}} = v_{\mathrm{p,bg}} \times J_{\mathrm{hom}}(T, S_{\mathrm{i}}) \times \Delta t \quad (2)$$

with the number concentration of homogeneously nucleated ice crystals $n_{\mathrm{i,hom}}$ (in cm^{-3}), the volume concentration for sulfate background aerosol $v_{\mathrm{p,bg}}$ (in cm^{-3} cm^{-3}), and the ice nucleation rate coefficient J_{hom} (in cm^{-3} s^{-1}) which is a function of temperature T and ice saturation ratio S_{i} (Koop et al., 2000). Here, we assume sulfate particles with radius of 50-100 nm. For computational details in the case of lidar application see Ansmann et al. (2021). The onset ice saturation ratio $S_{\mathrm{i,on}}$ is 1.5-1.6 in the case of homogeneous freezing. All available liquid background aerosol particles can be regarded as INPs (Heymsfield et al., 2017). According to airborne in situ observations of Schröder et al. (2002), conducted during the Lindenberg Aerosol Characterization Experiment 1998 (Ansmann et al., 2002), the number concentration of background sulfate particles is of the order of 250 cm^{-3} or 250000 L^{-1} in the upper troposphere and the respective volume concentration $v_{\mathrm{p,bg}}$, required in Eq. (2), is about 1.0 μm^3 cm^{-3}.

An updated approach to compute $n_{\mathrm{i,hom}}$ can be found in Koop and Zobrist (2009). According to previous studies (Knopf and Rigg, 2011; Riechers et al., 2013), J_{hom} in Eq. (2) is probably one to two orders of magnitude too large. However, our simulation show that this overestimation has only a minor impact on $n_{\mathrm{i,hom}}$. In the case of Arctic cirrus with ice nucleation temperatures around 200 K, the overestimation is of the order of 5%.

The concentration of nucleated ice cyrstals is finally given by the sum

$$n_{\mathrm{i}} = n_{\mathrm{i,het}} + n_{\mathrm{i,hom}}\,. \tag{3}$$

2.1.1 INP reservoir

The INP reservoir considers smoke particles with radius >250 nm in our simulations. The respective smoke particle number concentration n_{250} is estimated from lidar observations of the 532 nm particle extinction coefficient σ_{532} in the upper troposphere at cloud-free conditions (Ohneiser et al., 2021; Ansmann et al., 2023, 2025). Note that we use σ_{532} for the smoke aerosol extinction coefficient, here in part 2, and E for the ice crystal extinction coefficient in part 1.

According to the study of Ansmann et al. (2021), which deals with the conversion of lidar-derived smoke extinction coefficients (in Mm^{-1}) into microphysical properties of smoke particles, the surface area concentration s_{p} (in μm^2 cm^{-3}) and the large particle fraction n_{250} (in cm^{-3}) are given by

$$s_{\mathrm{p}} = c_{\mathrm{s}} \times \sigma_{532} \tag{4}$$

and

$$n_{250} = c_{250} \times \sigma_{532}\,. \tag{5}$$

with the extinction-to-surface-area conversion factor c_{s} (in Mm μm^2 cm^{-3}) and the extinction-to-particle-number conversion factor c_{250} (in Mm cm^{-3}). The values of c_{s} and c_{250} for aged wildfire smoke can be found in Ansmann et al. (2021). The link between s_{p} and n_{250} is simply given by

$$s_{\mathrm{p}} = \frac{c_{\mathrm{s}}}{c_{250}} \times n_{250}. \tag{6}$$

Eq. (6) is used in the simulation model to handle the INP reservoir (n_{250}), the decrease of n_{250} resulting from the nucleation of new ice crystals ($n_{\mathrm{i,het}}$) and the respective decrease of the surface area concentration s_{p}, used in the computation of $n_{\mathrm{i,het}}$ with Eq. (1). For aged wildfire smoke the ratio c_{s}/c_{250} is 5 μm^2 (Ansmann et al., 2021). The factor c_{s}/c_{250} can be interpreted as the average particle surface area of all particles of the large particle fraction (defined by n_{250}).

2.2 Ice crystal growth

The nucleated ice crystals grow by deposition of water vapor on the crystals. This process reduces the water vapor content in the air parcel and thus the ice saturation ratio S_{i}. If S_{i} decreases below the ice-nucleation threshold or onset level $S_{\mathrm{i,on}}$ or

$\mathrm{RH_{i,on}}$, ice nucleation will stop. The ice particle mass growth rate (for one crystal) is given by Lohmann et al. (2016)

$$\frac{\mathrm{d}q_\mathrm{i}}{\mathrm{d}t} = \frac{4\pi C_\mathrm{i}\,(S_\mathrm{i}-1)}{F_\mathrm{G}+F_\mathrm{H}}\,. \tag{7}$$

When assuming compact spherical ice crystals with radius r_i shortly after nucleation, instead of hexagonal plates or columns, the ice particle capacitance C_i (Westbrook et al., 2008) can be replaced by r_i. According to Skrotzki et al. (2013) this important simplification is justified. When expressing dq_i/dt by $4\pi r_\mathrm{i}^2 \rho_\mathrm{i}(dr_\mathrm{i}/dt)$ (Lohmann et al., 2016), we can compute the increase of the ice particle radius (in meter) within the simulation time step Δt,

$$\Delta r_\mathrm{i} = \frac{1}{r_\mathrm{i}}\frac{S_\mathrm{i}-1}{\rho_\mathrm{i}(F_\mathrm{G}+F_\mathrm{H})}\Delta t\,. \tag{8}$$

ρ_i is the bulk ice mass density (assumed to be 925 kg $\mathrm{m^{-3}}$). Eq. (8) is used in the computation of the mass growth term (Eq. 16).

The term F_G is related to the mass transfer of water molecules to the surface of the crystals (Skrotzki et al., 2013):

$$F_\mathrm{G} = \frac{R_\mathrm{w}T}{D_\mathrm{w}^* p_\mathrm{i,sat}} \tag{9}$$

with the specific gas constant of water vapor $R_\mathrm{w} = 461.5$ J $\mathrm{kg^{-1}}$ $\mathrm{K^{-1}}$ and the ice saturation pressure $p_\mathrm{i,sat}$ (in Pascal). Mass transfer of water molecules to the surface of the ice crystals is considered via the so-called modified version of water vapor diffusivity D_w^* (Skrotzki et al., 2013). D_w^* is given by

$$D_\mathrm{w}^* = D_\mathrm{w}\left(\frac{r_\mathrm{i}}{r_\mathrm{i}+\Delta_\mathrm{w}} + \frac{4D_\mathrm{w}}{\alpha_\mathrm{i} r_\mathrm{i} v_\mathrm{w}}\right)^{-1} \tag{10}$$

with the water vapor diffusivity,

$$D_\mathrm{w} = 2.11\times10^{-5}\left(\frac{T}{T_0}\right)^{1.94}\frac{p_0}{p}\,, \tag{11}$$

where T and p are air temperature and pressure, respectively, and $T_0 = 273$ K and $p_0 = 1013$ hPa. Δ_w in Eq. (10) is the so-called water vapor jump length which is often chosen to be of the order of the mean free path λ_w (in meter) of the water vapor molecules in air, so that we use $\lambda_\mathrm{w} \approx \Delta_\mathrm{w}$ (Skrotzki et al., 2013). The mean free path λ_w is given by

$$\lambda_\mathrm{w} = k_\mathrm{B}T\left(\pi p\left(\frac{\sigma_\mathrm{w}+\sigma_\mathrm{a}}{2}\right)^2\sqrt{1+\frac{M_\mathrm{w,mol}}{M_\mathrm{a,mol}}}\right)^{-1} \tag{12}$$

with the Boltzmann constant k_B, the collision diameters of a water vapor molecule σ_w (about 0.27 nm) and of an air molecule σ_a (about 0.37 nm), and molar mass of water $M_\mathrm{w,mol}$ and of air $M_\mathrm{a,mol}$. In short, $\lambda_\mathrm{w} = 3.371\times10^{-5}\times T/p$ with temperature in Kelvin and pressure in Pascal. The thermal velocity (in m $\mathrm{s^{-1}}$) in Eq. (10) is given by

$$v_\mathrm{w} = \sqrt{\frac{8R_\mathrm{w}T}{\pi}}\,, \tag{13}$$

in short $v_\mathrm{w} = 34.28\sqrt{T}$. Finally, the accommodation coefficient or deposition coefficient α_i (Skrotzki et al., 2013) in Eq. (10) must be given as input and is set constant. Reasonable values are 0.5-1.0. Skrotzki et al. (2013) recommended a deposition

growth coefficient of 1.0. Kärcher et al. (2022, 2023) introduced a complex scheme to compute $\alpha_{\rm i}$ as function of crystal size and ice saturation ratio $S_{\rm i}$. The approach is based on sophisticated laboratory investigations discussed in the articles. The discussions in Kärcher et al. (2023) emphasizes that further work is needed in this complex field of research. We follow Spichtinger et al. (2023) and set $\alpha_{\rm i} = 0.5$.

The thermodynamic term $F_{\rm H}$ in Eqs. (7) and (8) is related to latent heat release due to the diffusion of heat away from the ice crystal (Lohmann et al., 2016):

$$F_{\rm H} = \left(\frac{L_{\rm s}}{R_{\rm w} T} - 1 \right) \frac{L_{\rm s}}{K T} \tag{14}$$

with $L_{\rm s} = 2.836 \times 10^6$ J kg^{-1} (denoted as heat of sublimation) and the thermal conductivity coefficient (in J m^{-1} s^{-1} K^{-1}),

$$K = 4.1868 \times 10^{-3} [5.69 + 0.017 (T - 273.15)] \,. \tag{15}$$

$F_{\rm H}$ contributes to the sum $F_{\rm G} + F_{\rm H}$ by <5% for temperatures <235 K and is thus of low importance.

In the following, we explain the successive steps in the simulations of the MOSAiC ice nucleation events. The starting height z_0 of the simulations is set into the top region of the cirrus (the coldest part of the cloud with highest ice saturation ratio). In the case of a simulated gravity wave, the air parcel will be lofted from z_0 to $z_0 + A_{\rm GW}$, with the amplitude of the gravity wave $A_{\rm GW}$, and will then descend to $z_0 - A_{\rm GW}$ before returning to z_0. We also simulated large-scale lofting events from z_0 to $z_0 + 300$ m and constant updraft speed of 1-3 cm s^{-1} .

In Fig. 1, the calculation steps j and $j+1$ after exceeding the threshold or onset ice saturation level $S_{\rm i,on}$ for heterogeneous or homogeneous ice nucleation are shown. As long as the threshold relative humidity RH$_{\rm i,on}$ is not reached, the simulated air parcel just ascends with the given vertical velocity and $n_{\rm i}$ remains zero. The number of ice crystals that nucleated in step j (after exceeding the onset $S_{\rm i,on}$) is given by $n_{\rm i}(j)$ (see Eqs. 1-3). All earlier formed ice crystals (formed during foregoing time steps, indicated by index l ($l < j$) from 1 to $j-1$ in Eq. 16) remain in the air parcel during the entire ascent and permanently grow by water vapor uptake. The consideration of sedimentation aspects is discussed in Sect. 2.3. The time given for ice crystals, which nucleated in the earlier step l, to grow is $(j-l) \times \Delta t$. This means, the older the crystals, the larger they are according to Eqs. (7) and (8) in the computations of ice mass growth in step $j_{\rm step} = j$. By this process of continuous deposition of water vapor on the crystals in super saturated air a broad crystal size spectrum develops with time.

The ice mass $Q_{\rm i}(j)$ (in kg m^{-3}) produced within the time interval $\Delta t(j)$ (see first red box in Fig. 1) is given by

$$Q_{\rm i}(j) = \frac{4\pi}{3} \rho_{\rm i} n_{\rm i}(j) [r_{\rm i}(j)^3 - r_{\rm INP}^3] + \sum_{l=1}^{j-1} \frac{4\pi}{3} \rho_{\rm i} n_{\rm i}(l) [r_{\rm i}(j,l)^3 - r_{\rm i}(j-1,l)^3] \tag{16}$$

with the bulk ice mass density $\rho_{\rm i}$ in kg m^{-3}, the ice crystal number concentration $n_{\rm i}$ in m^{-3}, and $r_{\rm i}$ in meter. For simplicity, the core mass density of an INP with radius r$_{\rm INP}$ (set to 0.25 μm) in Eq. (16) is assumed to be equal to $\rho_{\rm i}$. The increase of the crystal radius $r_{\rm i}(j)$ by $\Delta r_{\rm i}$ within time step $\Delta t(j)$ is computed by using Eq. (8).

In the next step, the ice mass $Q_{\rm i}(j)$ that formed during the time interval $\Delta t(j)$ must be subtracted from the absolute humidity (in kg m^{-3}) in the air parcel,

$$q_{\rm w} = \frac{p_{\rm w}}{R_{\rm w} T} \,, \tag{17}$$

to obtain the absolute humidity after ice growth in step j,

$$q_{\mathrm{w,G}}(j) = q_{\mathrm{w}}(j) - Q_{\mathrm{i}}(j)\,. \tag{18}$$

Furthermore, the heat release resulting from the water vapor deposition on the ice embryos and growing ice crystals, increases the temperature (Spichtinger et al., 2023),

$$T_{\mathrm{H}}(j) = T(j) + Q_{\mathrm{i}}(j) \times L_{\mathrm{s}}/c_{\mathrm{p}}\,. \tag{19}$$

The air pressure $p(j)$ (in Pascal) is influenced via the dependence of the barometric formula on the ambient temperature $T_{\mathrm{H}}(j)$ so that we introduce $p_{\mathrm{H}}(j)$ in Fig. 1. Then, we step forward and compute the water vapor pressure $p_{\mathrm{w,G,H}}(j)$ after ice growth (index G) and heat release (index H) by using Eq. (17),

$$p_{\mathrm{w,G,H}}(j) = q_{\mathrm{w,G}}(j) \times R_{\mathrm{w}} T_{\mathrm{H}}(j)\,. \tag{20}$$

The respective water vapor mixing ratio ($\mathrm{MR_{G,H}}$ in Fig. 1) is given by $0.622 \times p_{\mathrm{w,G,H}}(j)/[p_{\mathrm{H}}(j) - p_{\mathrm{w,G,H}}(j)]$, and the ice saturation ratio, affected by ice crystal growth and related water vapor loss, can be written as (cf. Eq. 18)

$$S_{\mathrm{i,G,H}}(j) = \frac{[q_{\mathrm{w}}(j) - Q_{\mathrm{i}}(j)] \times R_{\mathrm{w}} T_{\mathrm{H}}(j)}{p_{\mathrm{i,sat}}}\,. \tag{21}$$

The values of $p_{\mathrm{w,G,H}}$ are $p_{\mathrm{i,sat}}$ are given in Pascal.

The consideration of the removal of ice crystals from the air parcel by crystal sedimentation processes (Sect. 2.3) would influence the ice mass production and the mixing ratio reduction. This impact of sedimentation is indicted by index S in Fig. 1.

After the computation of ice nucleation, crystal growth, and potential sedimentation-related crystal losses (red boxes in Fig. 1), the next step of adiabatic lofting is simulated (blue boxes in Fig. 1). The water vapor mixing ratio $\mathrm{MR_{G,H,S}}$ is again constant during this computation of adiabatic lofting.

2.3 Sedimentation of ice crystals

As a result of ice growth, sedimentation processes come into play. Crystals start to fall and the larger ones (with significant sedimentation speed) will leave the air parcel and will thus no longer contribute to ice growth effects in the simulated, ascending air parcel. Spichtinger and Gierens (2009) and Spichtinger and Cziczo (2010) introduced comprehensive sedimentation schemes that consider the ice crystal size spectrum and size-resolved fall velocities. This approach was applied in cirrus simulations of Krämer et al. (2016).

In our simulation, we simply assume that all particles with $r_{\mathrm{i}}(j) > 10$ μm leave the air parcel. Ice crystals are no longer considered in the mass computation with Eq. (16) if the radius exceeds this threshold value. Khvorostyanov and Curry (2005) showed that ice crystals with radius of 5, 10, and 15 μm may fall with velocities of 5-10 cm s^{-1}, 10-15 cm s^{-1}, and 15-20 cm s^{-1} in the upper troposphere at temperatures below -40°C, respectively. During an ice nucleation event of, e.g., 300 s, particles with radius of 10 μm can therefore reach heights of 30-45 m below the height where they were nucleated. However,

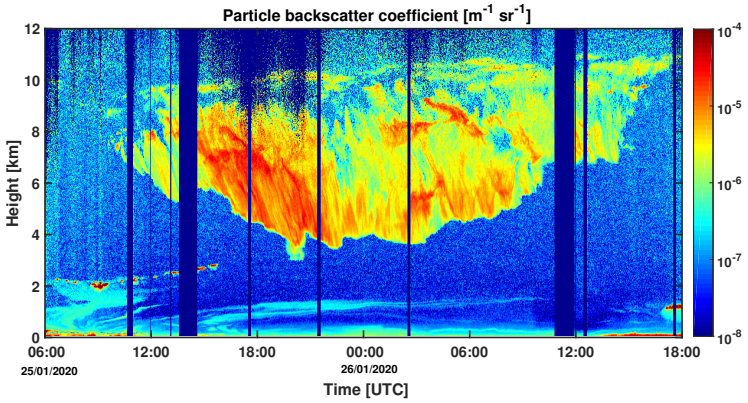

Figure 2. Cirrus life cycle observed with lidar over *Polarstern* at 87.4°N and 93-94°E on 25-26 January 2020. The cirrus (in light green, yellow and red colors) belongs to the synoptic cirrus category (top down generation of cirrus structures) (Lynch2002). The cirrus top layer (ice nucleation zone) ascended from about 9.8 to 11 km within 33 hours. Ice crystal virga of falling ice crystals reached down to 4 km height. Sublimation of crystals determine the lower rim of the virga zone. The particle backscatter coefficient at 1064 nm is shown. Multiplication of the backscatter coefficients with a cirrus lidar ratio of 30 sr yields the cirrus extinction coefficient.

the simulations showed that sedimentation processes at temperatures of -60 to -75°C (typical MOSAiC cirrus top temperatures) have almost no influence on ice nucleation events (in simulations of short-term gravity-wave-induced air parcel lofting). Because of the rather slow growth of ice crystals at temperatures around -70°C, crystal sizes remain mostly below 20 μm (in diameter) so that the sedimentation-related removal of crystals from the simulated air parcel has almost no impact on the simulation results.

Our simple sedimentation scheme allows us to simulate the maximum possible impact of sedimentation. The minimum impact is simulated by switching off the sedimentation routine. To match roughly the sedimentation-related impact on ice nucleation as simulated by Spichtinger and Cziczo (2010), we have to set the sedimentation threshold radius to 25-35 μm instead of the used radius of 10μm.

3 MOSAiC aerosol and cirrus observations: key findings

In Figs. 2-5, we provide a brief overview of key findings regarding smoke and cirrus properties during the MOSAiC winter half year 2019-2020. An extended discussion was given in part 1. Fig. 2 shows a complete life cycle of an Arctic cirrus cloud system, observed on 25-26 January 2020 during a six-day-long cirrus period (21-26 January 2020). Two other cirrus events of this long-lasting period, observed on 21-22 January 2020, were discussed in part 1 (Ansmann et al., 2025). The meteorological conditions measured with radiosondes, launched every six hours, and the cirrus properties observed with lidar and radar during the 21-26 January 2020 period served as a guide and orientation in our effort to design realistic smoke and cirrus simulation scenarios.

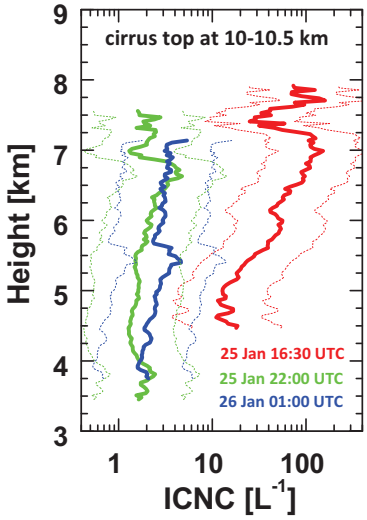

Figure 3. Ice crystal number concentration (ICNC, one hour mean profiles, begin of the measurement period is given in the panel), retrieved from combined lidar-radar observations in the virga height range on 25-26 January 2020 (see Fig. 2). Ice nucleation usually starts at cirrus top which was at heights >10 km on 25-26 January. The ICNC retrieval uncertainty range is indicated by thin dashed lines.

Large-scale lofting over 30 hours caused an ascent of the cirrus top layer from about 9.5 km to 11 km height (with a mean lofting velocity of about 1.5 cm s^{-1}) on 25-26 January 2020. Extended virga reached down to about 4 km height above *Polarstern*. The cirrus top temperature and ice saturation ratio were $T = -72°C$ and $S_i = 1.36$ at the beginning of the cirrus event (according to the observations with radiosonde launched at 5 UTC on 25 January). Later on the temperatures decreased to $-75°C$ and the ice saturation ratios ranged from 1.25 to 1.32 just below the tropopause. As mentioned before, ice nucleation preferably takes place in the coldest region of the cirrus layer and thus close to the top of the cirrus field.

Figure 3 shows one-hour mean ICNC height profiles derived from combined lidar and radar observations in extended virga fields on 25-26 January 2020. The retrieval is explaind in Ansmann et al. (2025). The three ICNC profiles cover well the range of MOSAiC ICNC values. In the majority of the observations, the virga ICNC values were between 1 and 10 L^{-1}, in many cases also between 10 and 50 L^{-1}. However, values >100 L^{-1} were rare. It was mentioned in part 1 (Ansmann et al., 2025), that the virga observations (geometrical structures, frequency of occurrence, ICNC) contain information about the strength (amplitude, duration) and occurrence frequency of individual updraft events and thus about the respective strength of the ice nucleation processes. The generally observed high virga occurrence frequency suggested that short-term updrafts events (and not large-scale lofting events) mainly contributed to ice nucleation in the observed cirrus clouds during the MOSAiC expedition.

Figure 4 shows an important MOSAiC finding, which is unfortunately not easy to identify in the height-time display of the shown lidar backscatter signal. As extensively discussed in Ohneiser et al. (2021) and Ansmann et al. (2023, 2024),

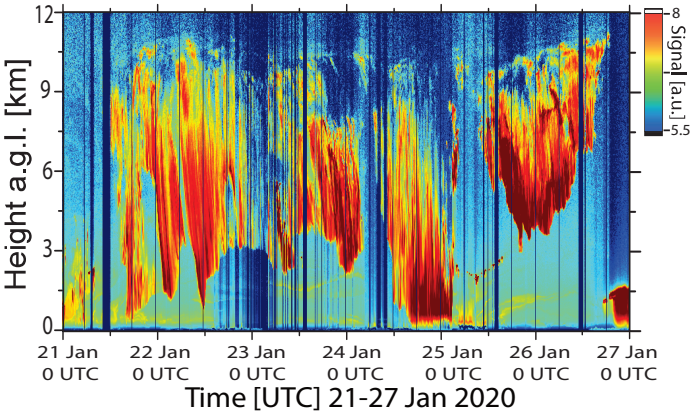

Figure 4. Lidar observations of smoke (in weak yellow) at heights around 10.5 km during a six-day-long cirrus period, lasting from 21-26 January 2020. Ice crystal fall strikes (virga in orange and red) are visible, mainly from 10 km down to 1-3 km height. Aged wildfire smoke was continuously observed during cloud-free periods above 6 km height during the entire MOSAiC winter half year (Ohneiser et al., 2021) with maximum pollution levels around or just above the tropopause. The height-time display of the range-corrected 1064 nm lidar return signal in logarithmic scales (a.u.: arbitray units) is presented.

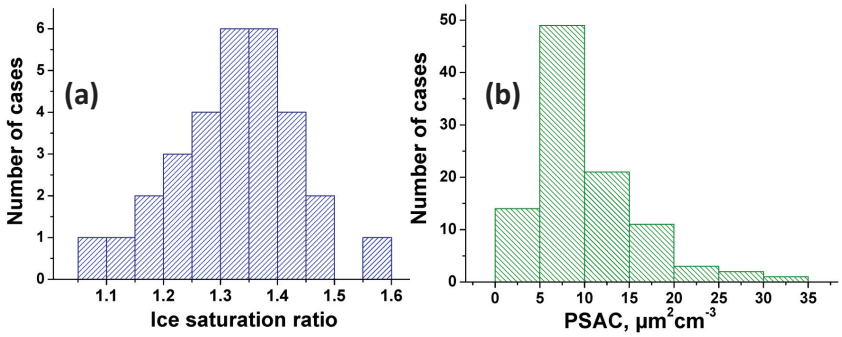

Figure 5. (a) Frequency of occurrence of the maximum ice saturation ratio measured with radiosondes in extended cirrus fields. Thirty radiosonde profiles were analyzed (November 2019 to February 2020). The maximum highest were usually measured close to the top of the cirrus layers. (b) Frequency of occurrence of the smoke particle surface area concentration (PSAC) derived from lidar observations at the tropopause during cirrus-free conditions (November 2019 to February 2020).

we observed almost constant levels of wildfire smoke pollution in the UTLS over the central Arctic from October 2019 to mid-May 2020. As can be seen in Fig. 4, there was always smoke at heights around 10.5 km, i.e., within and above the cirrus top height range. Smoke particles were continuously detected from about 6 km up to 2-4 km above the local
305 **tropopause. A very clear and impressive observation of a series of cirrus evolution events, all of them initiated within the permanently polluted upper troposphere, was presented in Fig. 14 in Ansmann et al. (2023), observed during another**

long-lasting cirrus period from 25-29 February 2020. The simulations will show that homogeneous freezing is widely, if not fully suppressed, at such pollution conditions. The observation of the persistent UTLS smoke layer is probably our strongest and most convincing argument for the hypothesis that smoke controlled cirrus formation in the central Arctic during the full MOSAiC winter half year.

The histograms in Fig. 5 provide, finally, an overview regarding the maximum values of the ice saturation ratios, observed with radiosondes in extended cirrus fields and regarding the smoke pollution levels derived from the lidar observations. The histogram in Fig. 5a is based on the analysis of 30 MOSAiC radiosonde observations performed during four months (November 2019 to February 2020). A careful inspection of each of the used radiosonde profiles in combination with the corresponding cirrus lidar observations clearly revealed that all of the 30 sondes ascended through cirrus layers. The cirrus backscatter profile signatures, observed with lidar, were usually in perfect agreement with the respective radiosonde RH and temperature profile signatures. The maximum ice saturation ratios S_i values accumulated between 1.3 and 1.4 in Fig. 5a and point to the dominance of heterogeneous ice nucleation on inefficient INPs as expected when organic particles serve as INPs. In Fig. 5b, the frequence-of-occurrence distribution of lidar-derived PSAC values observed during the winter months from November to February at the tropopause height level is given. In terms of the respective smoke particle extinction coefficients, the smoke perturbation caused 20 times higher extinction values than observed during undisturbed clean conditions. The humidity and pollution values in Fig. 5 and the ICNC profiles in Fig. 3 were used as orientation in the design of the simulation scenarios.

4 Simulation results

Main goal of the simulations was to provide a deeper insight further insight into the ability of smoke to influence ice formation at cirrus temperatures of -60 to -75°C and, more generally, to obtain a detailed view on the roles of heterogeneous and homogeneous ice nucleation in cirrus formation processes during the MOSAiC winter half year. We start with a scenario of large-scale lofting of air parcels, characterized by low lofting velocities of 1 and 3 cm s^{-1}. Next, we will discuss ice nucleation during short-term updraft events resulting from gravity wave activity. A typical lofting velocity of 20 cm s^{-1} is selected in these simulations. Of specific interest are those updraft conditions that lead to low ICNCs of < 50 L^{-1} as typically observed during the MOSAiC winter half year. Finally, the impact of a mixture of less efficient to very efficient smoke particles on ice formation is illuminated.

We use similar start conditions for the ascending air parcels in most simulations to facilitate comparison of different simulation scenarios. All lofting simulations start with an ice saturation ratio $S_\mathrm{i}(z_0) = 1.2$ at the starting height z_0. Simulations with a temperature of $T(z_0) = 199$ K at $z_0 = 10.5$ km represent cirrus formation conditions usually observed in January and February 2020 and simulations with a temperature of $T(z_0) = 213$ K at $z_0 = 9$ km reflect the cirrus formation conditions usually observed in November and December 2019. Table 1 contains the smoke input data (particle surface area concentration s_p, volume concentration $v_\mathrm{p,bg}$ at background aerosol conditions, number concentration n_{250} of large smoke particles) and the input data for the cold Arctic cirrus scenario ($T = 199$ K, $p = 212$ hPa, RH=64% at the

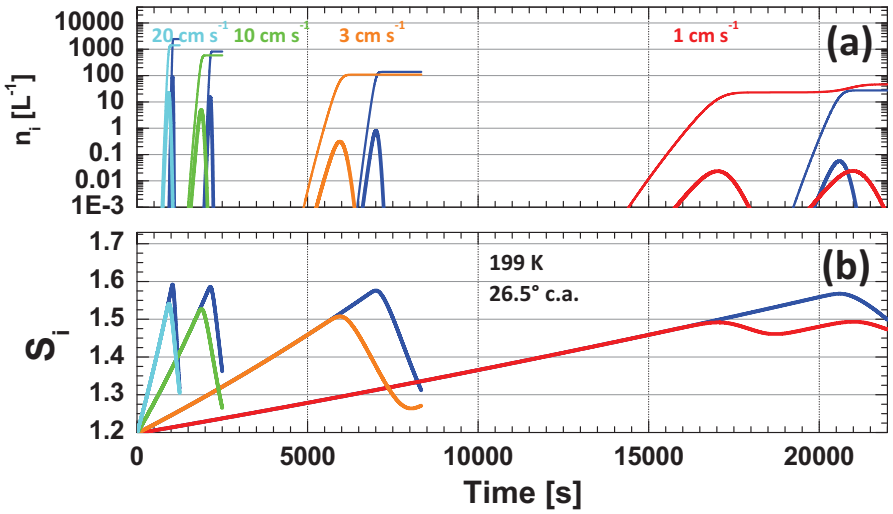

Figure 6. Simulation of deposition ice nucleation (DIN) on smoke INPs during the adiabatic rise of an air parcel ascending with constant updraft velocity of 1 cm s^{-1} (red), 3 cm s^{-1} (orange), 10 cm s^{-1} (green), and 20 cm s^{-1} (cyan). For comparison, homogeneous freezing of background aerosol particles (dark blue, at smoke-free conditions) is shown. Temperature $T(z_0)$ is 199 K and ice saturation ratio $S_\mathrm{i}(z_0)$ is 1.2 for all scenarios at the start of the ascent at height z_0. (a) Temporal evolution of the ice crystal number concentration $n_\mathrm{i} = n_\mathrm{i,het}$ and $n_\mathrm{i} = n_\mathrm{i,hom}$ (number of crystals nucleated within $\Delta t = 1$ s), and (b) temporal evolution of the ice saturation ratio S_i. Thick solid lines in (a) show n_i, thin lines the sum $\sum n_\mathrm{i}$ of all nucleated crystals. The strong drop in the S_i values is caused by ice crystal growth. Simulated sedimentation effects lead to two ice nucleation events in the case of the updraft velocity of 1 cm s^{-1} (in red). Time resolution in the simulation is 0.1 s, 0.5 s, and 1 s for the scenarios with lofting velocities of 10 and 20 cm s^{-1}, 3 cm s^{-1}, and 1 cm s^{-1}, respectively.

starting height $z_0 = 10.5$ km, $c_\mathrm{angle} = 26.5°$) and the warm Arctic cirrus scenario ($T = 213$ K, $p = 265$ hPa, RH=69.5% at the starting height $z_0 = 9$ km, $c_\mathrm{angle} = 24.5°$).

4.1 Ice nucleation during large-scale lofting

In Fig. 6, two large-scale lofting scenarios with low ascend velocities of 1 and 3 cm s^{-1} are presented. In addition, simulations with constant vertical velocities of 10 and 20 cm s^{-1} are included to show the dependence of ice nucleation on ascent speed. An ice-nucleation event at cold cirrus conditions (as observed on 22 January 2020, part 1, or on 25-26 January, Fig. 2) is simulated. We compare scenarios of heterogeneous ice nucleation on smoke particles with respective homogeneous freezing scenarios for background aerosol conditions. In the latter simulations, the smoke particle number concentration is set to zero.

All simulations show burst-like ice nucleation events. These well defined events are the result of the interplay of two processes (causing opposite effects). The ascent of the air parcel leads to a monotonic increase of the ice saturation ratio S_i, and when the onset value $S_\mathrm{i,on}$ is reached and exceeded, ice nucleation sets in. On the other hand, the growth

of ice particles by deposition of water vapor on the ice crystal surfaces reduces the water vapor in the ascending air parcel. The ice saturation ratio $S_{\rm i}$ decreases according to Eq. (21). When $S_{\rm i}$ drops below the onset value $S_{\rm i,on}$ again, ice nucleation stops.

In our study, the onset ice saturation ratio $S_{\rm i,on}$ is defined by the ice saturation ratio $S_{\rm i}$ for which the ice crystal number concentration, $n_{\rm i,hom}$ or $n_{\rm i,het}$, nucleated within $\Delta t = 1$ s, exceeds (for the first time) the value of 0.001 $\rm L^{-1}$ in an ascending air parcel. The onset ice saturation ratios are $S_{\rm i,on} = 1.556$ and 1.474 for homogeneous and heterogeneous ice nucleation at 199 K, respectively.

The consideration of crystal sedimentation by applying our simplified sedimentation approach, outlined in Sect. 2.3, leads to a second nucleation event in the scenario with 1 cm $\rm s^{-1}$ ascent rate (in red in Fig. 6). Similar sedimentation-related features occur in the other simulations, but they are not shown in Fig. 6. The second event is related to the fact that ice crystals with radius >10 μm are removed from the air parcel in the simulation and do no longer contribute to the reduction of the ice saturation ratio by growth of ice crystals. During the further ascent of the simulated air parcel at a reduced impact of ice growth the ice saturation starts to rise again and to exceed the onset value $S_{\rm i,on}$ for heterogeneous ice nucleation again, so that another burst-like structure shows up. Similar recurring ice nucleation features caused by the sedimentation impact were shown and discussed by Spichtinger and Cziczo (2010) and Krämer et al. (2016).

The main message of Fig. 6 is that wildfire smoke PSAC values of the order of 10 $\mu\rm m^2$ $\rm cm^{-3}$ and respective n_{250} values around 2000 $\rm L^{-1}$ as observed during the MOSAiC winter half year, are high enough to cause strong events of heterogeneous ice nucleation and to prevent homogeneous freezing. In all four simulation pairs with different vertical velocities, the ice nucleation onset ice saturation ratio $S_{\rm i,on}$ is lower in the case of smoke-induced heterogeneous ice nucleation than the respective $S_{\rm i,on}$ value for homogeneous freezing of background aerosol particles (see Fig. 6b). That means, that ice nucleation on smoke particles can start earlier in a rising air parcel than homogeneous freezing, and before the onset ice saturation ratio for homogeneous freezing is reached during the further ascent of the air parcel, growth of the already formed ice crystals strongly reduce the water vapor pressure (see Fig. 6b) so that the onset value $S_{\rm i,on}$ for homogeneous freezing cannot be reached anymore and therefore homogeneous ice nucleation will be completely suppressed as long as INPs are available in the rising air parcel. If the INP reservoir is empty, $S_{\rm i}$ can further increase at the almost unlimited rising conditions during a large-scale lofting events, and finally homogeneous freezing events can occur and dominate the further cirrus evolution. The question arises, how reasonable is the assumption that homogeneous can dominate ice formation in a highly and constantly polluted upper troposphere with an almost unlimited INP reservoir continuously refilled from the lower stratosphere? Homogeneous ice nucleation needs absolutely INP-free conditions so that freezing of background aerosol particles becomes a realistic option.

By comparing the simulations with different ascent velocities we see a strong impact of the vertical velocity on the total numbers of nucleated ice crystals, $\sum n_{\rm i,het}$ and $\sum n_{\rm i,hom}$. The integrated ICNC values are <50 $\rm L^{-1}$ in Fig. 6a for a typical synoptic ascent rate of 1 cm $\rm s^{-1}$. The numbers increase with increasing vertical velocity and are of the order of 100 $\rm L^{-1}$ (vertical velocity of 3 cm $\rm s^{-1}$), 1000 $\rm L^{-1}$(vertical velocity of 10 cm $\rm s^{-1}$), and even exceed 2000 $\rm L^{-1}$ (vertical velocity of 20 cm $\rm s^{-1}$). The higher the vertical velocity, the higher the (maximum) $S_{\rm i}$ value, reached in the rising air

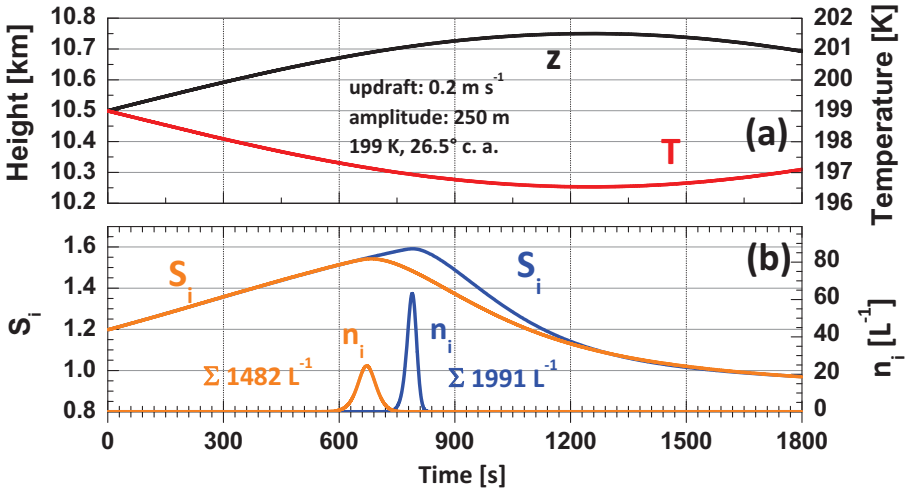

Figure 7. Heterogeneous ice nucleation (orange n_i curve in panel b) and homogeneous ice nucleation (blue n_i curve in panel b) during the ascent of a smoke-filled and smoke-free air parcel, respectively, along the black z curve in panel a. The upward motion is caused by a gravity wave, characterized by an updraft mean vertical velocity of 0.2 m s^{-1} (during the first quarter of the wave period) and a wave amplitude of 250 m. The temperature T (red curve in panel a) is 199 K at the starting height $z_0 = 10.5$ km, and the ice saturation ratio S_i at z_0 is 1.2 in panel b). The ice crystal number concentration n_i, nucleated in $\Delta t = 1$ s, is shown together with the sum $\sum n_\mathrm{i}$ of all heterogeneously or homogeneously nucleated ice crystals (given as numbers in panel b). Temporal resolution in the simulations is 0.1 s.

parcel, and the higher the respective maximum ice crystal number concentrations (thick solid lines in Fig. 6a) before the growth of the nucleated ice crystals becomes strong enough to terminate the nucleation event. This result is not new and was already shown in many publications before (see, e.g., Kärcher and Lohmann, 2002).

4.2 Gravity-wave-induced ice nucleation

The MOSAiC observations indicate that large-scale lofting occurred (as shown in Fig. 2) and may have contributed to cirrus formation. However, the observed high virga occurrence frequency suggested that short-term updraft events resulting from, e.g., gravity wave activity (Podglajen et al., 2016) dominated and triggered most of the observed ice nucleation events. Figure 7 shows a simulation scenario with ice nucleation initiated during the updraft phase of a gravity wave. A typical updraft-mean vertical velocity of 0.2 m s^{-1} (during the first quarter of the wave) and a relatively large GW amplitude of 250 m is simulated. Again, we compare heterogeneous ice nucleation in a smoke-filled air parcel with a respective homogeneous freezing event (at pure background aerosol conditions). As in the large-scale lofting simulation, homogeneous freezing will be suppressed as long as smoke INPs are available in the simulated air parcel because of the higher threshold, $S_\mathrm{i,on}$, required to start homogeneous freezing.

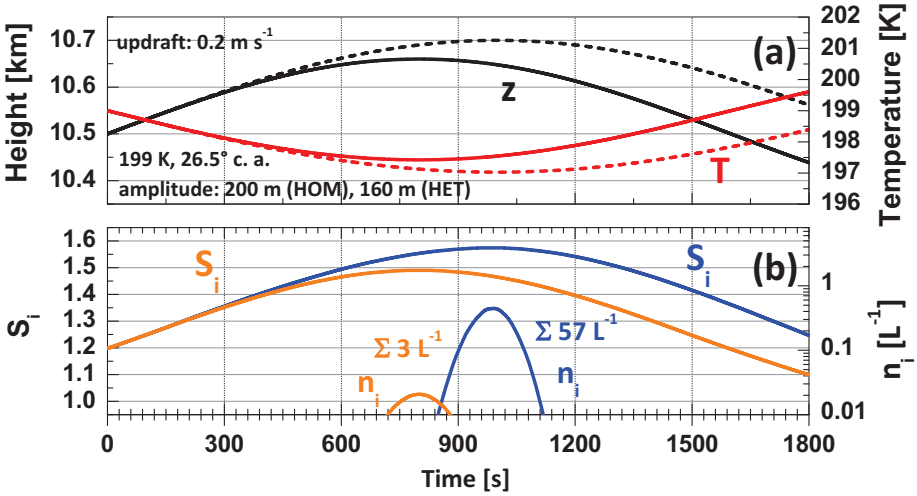

Figure 8. Same as Fig. 7, except for lower GW amplitudes of 200 m (homogeneous freezing, dashed curves in panel a) and 160 m (DIN, solid curves in panel a). In panel b, orange and blue curves indicate simulations of heterogeneous and homogeneous ice nucleation, respectively. As in Fig. 7, the ice crystal number concentration n_i, nucleated in $\Delta t = 1$ s, is shown together with the sum $\sum n_\mathrm{i}$ of all heterogeneously or homogeneously nucleated ice crystals (given as numbers in panel b).

The simulated large updraft amplitude of 250 m in combination with an ascent velocity of 20 cm s^{-1} provide favorable conditions for strong ice nucleation. Significant DIN begins after 600 s ($n_\mathrm{i} > 0.001$ L^{-1} s^{-1}, orange curve in Fig. 6b) when the onset ice saturation ratio $S_\mathrm{i,on} = 1.474$ is exceeded. The nucleation period stops about 120 s later when S_i drops below $S_\mathrm{i,on}$ again. The sum $\sum n_\mathrm{i,het}$ of all heterogeneously nucleated ice crystals is 1482 L^{-1}. The respective homogeneous freezing event needs higher super saturation ratios ($S_\mathrm{i,on} = 1.556$) and, at the end, produces more ice crystals ($\sum n_\mathrm{i,hom} = 1991$ L^{-1}).

This scenario with a large wave amplitude probably provides the most favorable conditions that homogeneous freezing comes into play. The INP reservoir in a given air parcel may be empty after a few minutes so that homogeneous freezing can set in after further rise of the air parcel or during subsequent updraft events, experienced by the meanwhile INP-free air parcel. In case of such large amplitudes, the ice nucleation onset value $S_\mathrm{i,on}$ for both heterogeneous and homogeneous ice nucleation (at smoke-free conditions) can be easily reached and exceeded so that large ice particle production is possible in both ways of ice nucleation.

The simulations in Sects. 4.1 and 4.2 show that both ice-nucleation modes can lead to rather low and rather high ICNC values so that an identification of the ice nucleation mode based on ICNC values is not possible.

4.3 Ice nucleation in the case of low GW amplitudes

The high ICNC values of the order of 1500-2000 L^{-1} in Fig. 7 were, however, not observed during MOSAiC. In well-defined, well-resolved virga, indicating single, individual updraft events, we typically found ICNCs of 1-10 L^{-1}, frequently also 10-

50 L^{-1}, but only rarely >100 L^{-1}. In many cases, the observed ICNC profiles in the virga height range provided the clear impression that aggregation effects (leading to a significant reduction of ICNC with crystal falling time and thus decreasing height, see discussion in part 1) did not play a significant role so that the virga ICNC values, available at heights of 1-3 km below the ice nucleation cells at cirrus top, can be used as trustworthy estimates for the ICNCs at cirrus top.

In the next step, we reduced the updraft amplitude in order to obtain low ICNC ($\sum n_{\rm i}$) values, to be better in line with the MOSAiC observations (Ansmann et al., 2025). According to the superpressure balloon observations of Podglajen et al. (2016), updraft events with low amplitudes occur much more frequently at UTLS heights in polar regions than strong updrafts (with large amplitudes). The observations of Podglajen et al. (2016) and the consequences for the observable ICNC levels ice nucleation processes in the central Arctis were discussed in detail in Sect.3.5 in part 1 (Ansmann et al., 2025). Besides a decrease of the amplitude, and thus the height range, available for an air parcel to rise and to initiate ice nucleation, also the decrease of the vertical velocity leads to a reduction of ICNC as was shown in Sect. 4.1. (Podglajen et al., 2016) observed both that updrafts with low amplitude occur most frequently and that updrafts with low vertical velocity occur most frequently. In our study, the main focus is on the impact of the amplitude on ice nucleation to keep the discussion simple.

A simulation leading to low ICNC values is shown in Fig. 8. In the case of a GW amplitude of 160 m (and $S_{\rm i}(z_0) = 1.2$), a very low ICNC number of $\sum n_{\rm i,het} = 3$ L^{-1} is obtained in the simulation with a wildfire-polluted upper troposphere (orange $n_{\rm i}$ curve in Fig. 8b). After exceeding $S_{\rm i,on}$, only 10 m of further lofting remain for ice nucleation so that a strong burst-like ice nucleation event cannot evolve. Homogeneous freezing is completely suppressed in the simulation of a shallow updraft with 160 m amplitude. The ice saturation ratio $S_{\rm i}$ remains below $S_{\rm i,on}$ for homogeneous freezing. To initiate homogeneous freezing, amplitudes around 200 m are needed as simulated in Fig. 8 as well.

It is noteworthy to mention in this context that the simulation of an ascending air parcel, that contains no ice crystals at the beginning of a nucleation event (as discussed here) is even representative for cases with air parcels that contain already ice crystals before the (new) ice nucleation event starts. The so-called pre-existing ice effect (Kuebbeler et al., 2014) may prohibit any further heterogeneous and especially homogeneous ice nucleation events when the pre-existing ICNC >100 L^{-1} in the air parcel. However, the pre-existing ice effect plays a negligible role when the pre-existing ICNC is far below 100 L^{-1} as was typically the case during the MOSAiC winter half year.

Figures 7 and 8 show simulations for cold cirrus conditions as observed in January and February 2020. In November and December 2019, the cirrus developed at temperatures of $-60°$ to $-65°$C, and cirrus top heights were frequently at 8-9 km height. Such a scenario is shown in Fig. 9. With increasing temperature the onset $S_{\rm i}$ value decreases (Wang and Knopf, 2011). The increased ice activity at higher temperatures is considered in the INPC computation by selecting a contact angle of 24.5° (instead of 26.5° at 199 K). As can be seen, lower updraft amplitudes of 100-120 m are sufficient in the case of a higher cirrus top temperature to initiate ice nucleation on smoke particles. Homogeneous ice nucleation needs again amplitudes around 200 m before significant ice nucleation starts. The onset ice saturation ratios are $S_{\rm i,on} = 1.515$ and 1.349 for homogeneous and heterogeneous ice nucleation at 213 K, respectively.

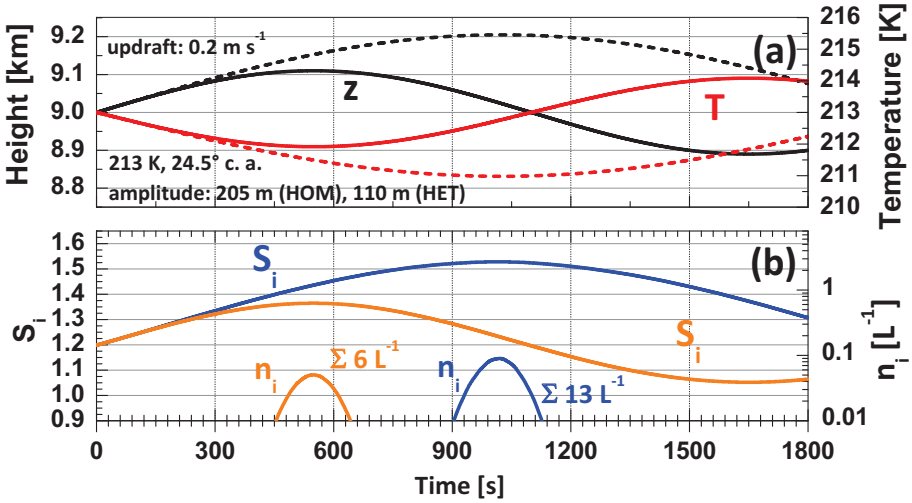

Figure 9. Same as Fig. 8, except for a warm Arctic cirrus with $T(z_0) = 213$ K at $z_0 = 9$ km, a lower contact angle of 24.5°, and amplitudes of 200 m (homogeneous freezing) and 110 m (heterogeneous ice nucleation). Again, the ice crystal number concentration n_i, nucleated in $\Delta t = 1$ s, is shown together with the sum $\sum n_\mathrm{i}$ of all heterogeneously or homogeneously nucleated ice crystals (given as numbers in panel b).

4.4 GW amplitude impact on ice nucleation: summary

Figure 10 finally shows the impact of the updraft amplitude on the accumulated number of nucleated ice crystals. As can be seen in Fig. 10, the number of totally nucleated ice crystals (ICNC) increases strongly with increasing updraft amplitude (for a given warm or cold cirrus scenario) as long as the amplitudes are small. ICNC is generally small <10 L^{-1} for relatively shallow updrafts. For updrafts with large amplitude, the dependence of ICNC on amplitude size is low. In the case of large amplitudes and a correspondingly large height range with $S_\mathrm{i} > S_\mathrm{i,on}$, strong ice nucleation as well as strong ice growth sets in. Even a large increase of the amplitude will not lead to a strong ICNC increase anymore.

According to the balloon observations of Podglajen et al. (2016) over Antarctica, described in detail in Sect. 3.5 in part 1, shallow updrafts occur always much more frequently than strong updrafts with relatively large amplitudes. Consequently, the observed ICNCs should be in most cases low because ice nucleation mainly occurs during updrafts having a low amplitude. This aspect may explain why most of the observed MOSAiC ICNC values are low.

Podglajen et al. (2016) also found a strong decrease of the frequency of occurrence for the updraft vertical velocity with increasing updraft speed. Small vertical velocities occur much more frequently than large vertical velocities. As discussed in Sect. 4.1, ICNC decreases with decreasing updraft mean vertical velocity. The findings of Podglajen et al. (2016) point again to the dominance of low ice crystal production so that, all in all, it is not surprising that most of the measured ICNC values were low in the Arctic cirrus clouds.

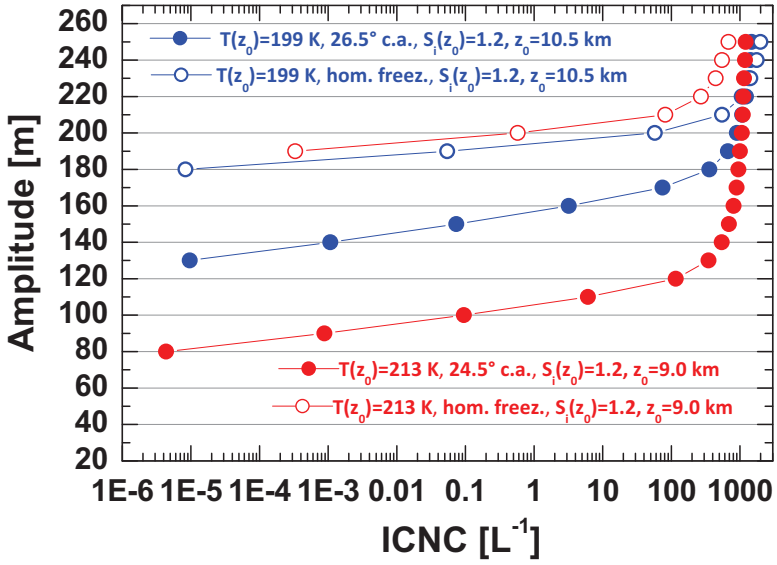

Figure 10. Impact of the gravity wave amplitude on the overall sum of heterogeneously nucleated ice crystals (ICNC, solid circles) for cirrus top temperatures of 199 K (in blue) and 213 K (in red). Homogeneous freezing scenarios (open circles) are shown for comparison. The mean updraft vertical velocity was set to 0.2 m s^{-1}.

When keeping the observations of typically low ICNCs of 1-50 L^{-1} in cirrus virga in mind together with the fact that the smoke INP reservoir was always well filled (and refilled from above) over the entire winter half year 2019-2020, it seems to be quite unrealistic to assume that homogeneous freezing significantly contributed to cirrus formation during the MOSAiC winter half year. Homogeneous freezing is possible in absolutely clean air only, i.e., at conditions with pure aerosol background conditions so that liquid sulfate particles of the background aerosol can start to when the respective onset ice saturation ratio $S_{\mathrm{i,on}}$ is reached and exceeded. Even if we assume a completely isolated air parcel (no exchange of aerosol particles and moisture with neighboring and polluted air parcels higher up), 10-50 short-term lofting events and respective heterogeneous ice nucleation events may be required before an initially smoke-filled air parcels is free of any smoke INP so that homogeneous ice nucleation can start.

We can further conclude from Fig. 10 in combination with the findings of Podglajen et al. (2016) that the conditions are always more favorable for heterogeneous ice nucleation than for homogeneous freezing. More opportunities for heterogeneous ice nucleation are given (because more shallow updrafts are available with amplitudes large enough to start ice nucleation) than for homogeneous ice nucleation, for which always amplitudes around 200 m are required before the onset ice saturation ratio is reached and ice nucleation can start.

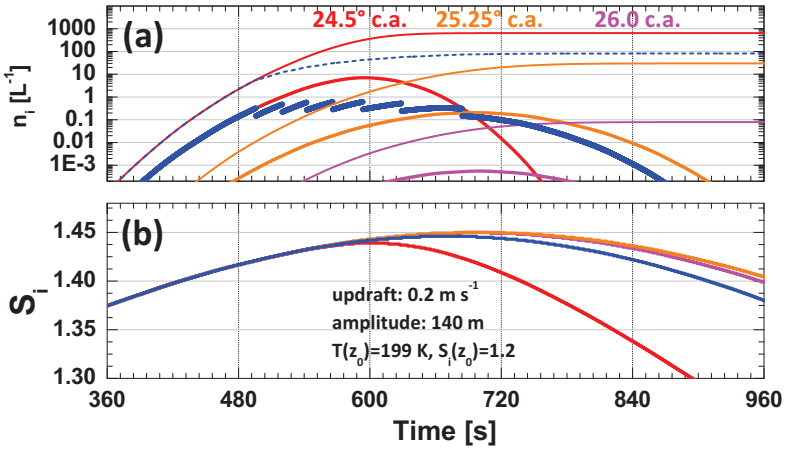

Figure 11. Ice nucleation scenario with a smoke aerosol mixture of efficient to inefficient INPs characterized by a broad contact angle distribution. A Gaussian distribution of contact angles (representing different ice-active smoke particle fractions) is simulated. $n_\mathrm{i} = n_\mathrm{i,het}$ is given as thick blue line segments, $\sum n_\mathrm{i}$ is given as blue dashed line. Cirrus with top temperature is 199 K, the updraft amplitude 140 m, and the updraft mean vertical velocity 0.2 m s^{-1}. The corresponding S_i curve (starting at 1.2 at z_0) is shown in (b) as thick blue line. For comparison the evolution of n_i (thick lines in a), $\sum n_\mathrm{i}$ (thin lines in a), and S_i (in b) for scenarios with a single contact angle of 24.5° (red), 25.25° (orange), and 26.0° (magenta) for the entire smoke particle population are shown.

4.5 Ice nucleation in the case of an aerosol mixture of efficient and inefficient smoke INPs

The final simulations focus on the impact of a mixture of relatively efficient to very inefficient smoke INPs on ice nucleation. Similar simulations with a mixture of less efficient to efficient dust INPs was presented by Kärcher et al. (2022). The aged wildfire smoke observed over the North Pole region from October 2019 to May 2020 was emitted into the atmosphere over Siberia in July-August 2019. After 3-10 months of long-range transport there may have been many fractions of organic aerosol particles with very different ice nucleation efficiencies, expressed by contact angles, e.g., from 24.5° (efficient INPs) to 29.5° (very inefficient INPs). To provide an impression of the ice activity of a complex aerosol mixture we defined a Gaussian distribution of 50 different smoke INP fractions, characterized by 50 different contact angles from 24.5° to 29.5°. The Gaussian distribution was centered at the INP fraction with a contact angle of 27.0°. The contact angle half width of the Gaussian distribution was 1.25°. The INP reservoir was set to $n_{250} = 2000$ L^{-1} as in the previous cases. By using this mixture, we compared the simulation runs with fixed, single contact angles of 24.5°, 25.25°, and 26.0° for all particles in the INP reservoir with the one for the mixture. The results are shown in Fig. 11.

In the case of the aerosol mixture, the smoke fraction with the highest ice nucleation efficiency is activated first. When this INP reservoir for the most ice-active fraction (24.5° c.a.) is depleted, the next fraction (24.6° c.a.) becomes ice-active, and so on. Note again, that the onset saturation ratio $S_\mathrm{i,on}$ is lowest for 24.5° and increases with increasing contact angle. In the case of a wave amplitude of 140 m, only a few INP fractions become activated (contact angles from 24.5°-25.2°). We can conclude

that heterogeneous ice nucleation is widely controlled by the most efficient INPs and that the inefficient INPs may not be activated at all.

5 Summary, conclusions, and outlook

Based on a dense set of aerosol and cirrus observations in the central Arctic over a half year (part 1) and accompanying ice nuclation simulations (part 2), we presented the first systematic study of the potential impact of wildfire smoke on cirrus formation. Since the number of major wildfire events increases since years and ground-based and spaceborne lidars detected a strong increase in the occurrence frequency of wildfire smoke in the UTLS height range since 2017, it is important to better understand the role of wildfire smoke in the atmospheric system in order to accurately consider wildfire smoke in atmospheric modelling and future climate research.

The observations in part 1 provided already a number of arguments for a strong impact of wildfire smoke on cirrus formation during the MOSAiC winter half year. We observed a persistent upper tropospheric INP reservoir that was continuously refilled by a downward flux of smoke particles from the stratosphere. This unlimited source of INPs is the cornerstone of our hypothesis that heterogeneous ice nucleation on smoke particles dominated and homogeneous freezing processes were widely suppressed. In terms of optical properties, the particle light-extinction coefficient was enhanced by a factor of 20 (due to the presence of smoke) compared to pure background aerosol extinction coefficients. As an independent indication (complementary to the lidar and radar observations) of a strong impact of smoke on cirrus formation, the MOSAiC radiosondes, ascending through extended cirrus fields, mainly measured maximum ice saturation ratios of 1.3-1.5. These maximum ice saturation ratios usually occurred in the uppermost part of the cirrus layers. They point to heterogeneous ice nucleation initiated by inefficient INPs as expected when glassy organic aerosol particles serve as INPs.

The simulation study in part 2 complemented the observation and confirmed the hypotheses on a strong impact of smoke on cirrus formation. The simulations allowed a much deeper view into the ice nucleation processes by considering ice nucleation, ice growth, heat release and sedimentation. Furthermore, rather different scenarios regarding air parcel lofting conditions can be studied based on simulations. For the first time, an INP reservoir was introduced in cirrus simulations by following the argumentation of Knopf et al. (2023a). The introduction of an INP reservoir also considers best the fact that high levels of smoke pollution were permanently observed with lidar in the upper troposphere during the first 7.5 months of the MOSAiC expedition.

The simulations confirmed that the measured PSAC values of about 10 ± 5 μm^2 cm^{-3} were high enough to initiate strong ice nucleation processes and to prevent homogeneous freezing. The simulations supported the hypothesis that ice nucleation is a strong function of the amplitude of the short-term updraft events. The lower the amplitude, the lower the number of nucleated ice crystals. Together with observations of Podglajen et al. (2016), indicating that shallow updrafts with low amplitudes occur much more frequently than strong updrafts with large amplitudes, the simulations are in good agreement with the MOSAiC observations that show most frequently quite low ICNCs. In summary, we found

many indication from observations and simulations that support the hypothesis that wildfire smoke played a strong role in central Arctic cirrus formation processes in the winter of 2019-2020. However, even in the case of a highly polluted UTLS we cannot completely rule out that occasionally situations occurred in which smoke-free conditions were given in a number of air parcels after the consumption of all INPs (after many updraft events) so that homogeneous freezing processes could start in these air parcels.

Disregarding the numerous arguments for a significant smoke impact on ice formation in the Arctic upper troposphere, a caveat of our study is that we do not know the exact deposition ice nucleation properties of wildfire smoke particles that aged over months of long range transport in the upper troposphere and lower stratosphere. INP-related laboratory studies for this special particle type are not available. We applied a deposition ice nucleation parameterization that reflects characteristics of organic particles derived from laboratory studies (Wang and Knopf, 2011; Wang et al., 2012). These organic surrogate INP particles possess a highly viscous including solid, phase state and oxygenated functional groups as would be expected for actual UTLS smoke particles (Knopf et al., 2018). It is unlikely that the ice nucleation efficiency of an organic smoke particle would be orders of magnitude different as studies on organic particles serving as INPs have shown (Murray et al., 2010; Knopf et al., 2018; Wolf et al., 2020). Clearly, more research including the collection of smoke particles and laboratory studies (e.g. Knopf et al., 2023b) and airborne in situ measurements (Cziczo et al., 2017) are required in this exciting field of atmospheric research.

As an outlook, we plan to extend our smoke-cirrus interaction studies. In the framework of the DACAPO-PESO (Dynamics, Aerosol, Cloud and Precipitation Observations in the Pristine Environment of the Southern Ocean) campaign in Punta Areans, southern Chile (Radenz et al., 2021), we continuously monitored smoke layers in the upper troposphere and the stratosphere in 2020 and 2021 originating from the record-breaking bushfires in eastern Australia in December 2019 and January 2020 (Ohneiser et al., 2020, 2022). Many cirrus layers developed in the polluted upper troposphere over the southernmost tip of South America, in the usually rather clean atmosphere over the Southern Ocean. A unique lidar-radar data set is thus available to explore the impact of the Australian smoke (from burning of eucalyptus trees) on midlatitude cirrus formation in the usually very clean southern hemisphere.

6 Data availability

Polly lidar observations (level 0 data, measured signals) are in the PollyNet database (Polly, 2024). All the analysis products are available at TROPOS upon request (polly@tropos.de) and at https://doi.pangaea.de/10.1594/PANGAEA.935539 (Ohneiser et al., 2021). Cloud radar data are downloaded from the ARM data base (ARM, 2024; ARM-MOSAiC, 2024). MOSAiC radiosonde data are available at https://doi.org/10.1594/PANGAEA.928656 (Maturilli et al., 2021, 2022). Products from synergistic lidar-radar studies and cirrus simulation results can be obtained on request (by contacting the corresponding author).

7 Author contributions

The paper was written and designed by AA and DAK, data analysis was performed by CJ, JR, JB, KO, and RE. AA developed the simulation model and produced the simulation results. All coauthors were actively involved in the extended discussions and the elaboration of the final design of the manuscript.

8 Competing interests

Daniel A. Knopf is a member of the editorial board of Atmospheric Chemistry and Physics

9 Financial support

The Multidisciplinary drifting Observatory for the Study of the Arctic Climate (MOSAiC) program was funded by the German Federal Ministry for Education and Research (BMBF) through financing the Alfred Wegener Institut Helmholtz Zentrum für Polar und Meeresforschung (AWI) and the *Polarstern* expedition PS122 under grant N-2014-H-060_Dethloff. The lidar analysis on smoke-cirrus interaction was further supported by BMBF funding of the SCiAMO project (MOSAIC-FKZ 03F0915A). The radiosonde program was funded by AWI awards AFMOSAiC-1_00 and AWI_PS122_00, the U.S. Department of Energy Atmospheric Radiation Measurement Program, and the German Weather Service. This project has also received funding from the European Union's Horizon 2020 research and innovation program ACTRIS-2 Integrating Activities (H2020-INFRAIA-2014 - 2015, grant agreement no. 654109) as well as from the European Union's Horizon Europe Programme under Grant Agreement No. 101137639 (CleanCloud). We gratefully acknowledge the funding by the Deutsche Forschungsgemeinschaft (DFG, German Research Foundation) – project no. 268020496 - TRR 172, within the Transregional Collaborative Research Center "ArctiC Amplification: Climate Relevant Atmospheric and SurfaCe Processes, and Feedback Mechanisms (AC)3". DAK acknowledges support by U.S. Department of Energy's (DOE) Atmospheric System Research (ASR) program, Office of Biological and Environmental Research (OBER) (grant no. DE-SC0021034).

Acknowledgements. Data used in this article were produced as part of the international Multidisciplinary drifting Observatory for the Study of the Arctic Climate (MOSAiC) with the tag MOSAiC20192020 and the Project_ID: AWI_PS122_00. We would like to thank everyone who contributed to the measurements used here (Nixdorf et al., 2021).

References

Ansmann, A., Wandinger, U., Wiedensohler, A., and Leiterer, U.: Lindenberg Aerosol Characterization Experiment 1998 (LACE 98): Overview, Journal of Geophysical Research: Atmospheres, 107, LAC 11–1–LAC 11–12, https://doi.org/10.1029/2000JD000233, 2002.

Ansmann, A., Ohneiser, K., Mamouri, R.-E., Knopf, D. A., Veselovskii, I., Baars, H., Engelmann, R., Foth, A., Jimenez, C., Seifert, P., and Barja, B.: Tropospheric and stratospheric wildfire smoke profiling with lidar: mass, surface area, CCN, and INP retrieval, Atmospheric Chemistry and Physics, 21, https://doi.org/10.5194/acp-21-9779-2021, 2021.

Ansmann, A., Ohneiser, K., Engelmann, R., Radenz, M., Griesche, H., Hofer, J., Althausen, D., Creamean, J. M., Boyer, M. C., Knopf, D. A., Dahlke, S., Maturilli, M., Gebauer, H., Bühl, J., Jimenez, C., Seifert, P., and Wandinger, U.: Annual cycle of aerosol properties over the central Arctic during MOSAiC 2019–2020 – light-extinction, CCN, and INP levels from the boundary layer to the tropopause, Atmospheric Chemistry and Physics, 23, 12 821–12 849, https://doi.org/10.5194/acp-23-12821-2023, 2023.

Ansmann, A., Veselovskii, I., Ohneiser, K., and Chudnovsky, A.: Comment on "Stratospheric Aerosol Composition Observed by the Atmospheric Chemistry Experiment Following the 2019 Raikoke Eruption" by Boone et al., Journal of Geophysical Research: Atmospheres, 129, e2022JD038 080, https://doi.org/https://doi.org/10.1029/2022JD038080, e2022JD038080 2022JD038080, 2024.

Ansmann, A., Jimenez, C., Roschke, J., Bühl, J., Ohneiser, K., Engelmann, R., Radenz, M., Griesche, H., Hofer, J., Althausen, D., Knopf, D. A., Dahlke, S., Maturilli, M., Gaudek, T., Seifert, P., and Wandinger, U.: Impact of wildfire smoke on Arctic cirrus formation, part 1: observations during MOSAiC 2019-2020, EGUsphere, 2024, 1–YYY, https://doi.org/10.5194/egusphere-2024-2008, 2025.

ARM-MOSAiC(2024): Atmospheric Radiation Measurement (ARM) user facility, 2019, updated hourly, Ka ARM Zenith Radar (KAZR-CFRGE), 2019-10-11 to 2020-09-20, ARM Mobile Facility (MOS) MOSAIC (Drifting Obs - Study of Arctic Climate), AMF2 (M1), compiled by I. Lindenmaier, D. Nelson, B. Isom, J. Hardin, A. Matthews, T. Wendler, and V. Castro, ARM Data Center, last access: 13 February, 2024.

ARM(2024): Atmospheric Radiation Measurement (ARM) user facility, data are collected through routine operations and scientific field experiments, US Department of Energy (DOE), available at https://arm.gov/data, last access: 22 January 2024, 2024.

Cziczo, D. J., Ladino, L., Boose, Y., Kanji, Z. A., Kupiszewski, P., Lance, S., Mertes, S., and Wex, H.: Measurements of Ice Nucleating Particles and Ice Residuals, Meteorological Monographs, 58, 8.1 – 8.13, https://doi.org/10.1175/AMSMONOGRAPHS-D-16-0008.1, 2017.

DeMott, P. J., Prenni, A. J., Liu, X., Kreidenweis, S. M., Petters, M. D., Twohy, C. H., Richardson, M. S., Eidhammer, T., and Rogers, D. C.: Predicting global atmospheric ice nuclei distributions and their impacts on climate, Proc. Natl. Acad. Sci. USA, 107, 11 217–11 222, https://doi.org/10.1073/pnas.0910818107, 2010.

Haag, W. and Kärcher, B.: The impact of aerosols and gravity waves on cirrus clouds at midlatitudes, Journal of Geophysical Research: Atmospheres, 109, https://doi.org/10.1029/2004JD004579, 2004.

Heymsfield, A. J., Krämer, M., Luebke, A., Brown, P., Cziczo, D. J., Franklin, C., Lawson, P., Lohmann, U., McFarquhar, G., Ulanowski, Z., and Tricht, K. V.: Cirrus Clouds, Meteorological Monographs, 58, 2.1 – 2.26, https://doi.org/10.1175/AMSMONOGRAPHS-D-16-0010.1, 2017.

Kanji, Z. A., Florea, O., and Abbatt, J. P. D.: Ice formation via deposition nucleation on mineral dust and organics: dependence of onset relative humidity on total particulate surface area, Environmental Research Letters, 3, 025 004, https://doi.org/10.1088/1748-9326/3/2/025004, 2008.

Khvorostyanov, V. I. and Curry, J. A.: Fall Velocities of Hydrometeors in the Atmosphere: Refinements to a Continuous Analytical Power Law, Journal of the Atmospheric Sciences, 62, 4343 – 4357, https://doi.org/10.1175/JAS3622.1, 2005.

Knopf, D. A. and Alpert, P. A.: A water activity based model of heterogeneous ice nucleation kinetics for freezing of water and aqueous solution droplets, Farad. Discuss., 165, 513–534, https://doi.org/10.1039/c3fd00035d, 2013.

Knopf, D. A. and Alpert, P. A.: Atmospheric ice nucleation, Nature Reviews Physics, 5, 203–217, https://doi.org/10.1038/s42254-023-00570-7, 2023.

Knopf, D. A. and Rigg, Y. J.: Homogeneous Ice Nucleation From Aqueous Inorganic/Organic Particles Representative of Biomass Burning: Water Activity, Freezing Temperatures, Nucleation Rates, The Journal of Physical Chemistry A, 115, 762–773, https://doi.org/10.1021/jp109171g, pMID: 21235213, 2011.

Knopf, D. A., Alpert, P. A., and Wang, B.: The role of organic aerosol in atmospheric ice nucleation: a review, ACS Earth and Space Chemistry, 2, 168–202, https://doi.org/10.1021/acsearthspacechem.7b00120, 2018.

Knopf, D. A., Silber, I., Riemer, N., Fridlind, A. M., and Ackerman, A. S.: A 1D Model for Nucleation of Ice From Aerosol Particles: An Application to a Mixed-Phase Arctic Stratus Cloud Layer, Journal of Advances in Modeling Earth Systems, 15, e2023MS003 663, https://doi.org/10.1029/2023MS003663, e2023MS003663 2023MS003663, 2023a.

Knopf, D. A., Wang, P., Wong, B., Tomlin, J. M., Veghte, D. P., Lata, N. N., China, S., Laskin, A., Moffet, R. C., Aller, J. Y., Marcus, M. A., and Wang, J.: Physicochemical characterization of free troposphere and marine boundary layer ice-nucleating particles collected by aircraft in the eastern North Atlantic, Atmospheric Chemistry and Physics, 23, 8659–8681, https://doi.org/10.5194/acp-23-8659-2023, 2023b.

Koop, T. and Zobrist, B.: Parameterizations for ice nucleation in biological and atmospheric systems, Phys. Chem. Chem. Phys., 11, 10 839–10 850, https://doi.org/10.1039/B914289D, 2009.

Koop, T., Luo, B. P., Tsias, A., and Peter, T.: Water activity as the determinant for homogeneous ice nucleation in aqueous solutions, Nature, 406, 611–614, https://doi.org/10.1038/35020537, 2000.

Krämer, M., Rolf, C., Luebke, A., Afchine, A., Spelten, N., Costa, A., Meyer, J., Zöger, M., Smith, J., Herman, R. L., Buchholz, B., Ebert, V., Baumgardner, D., Borrmann, S., Klingebiel, M., and Avallone, L.: A microphysics guide to cirrus clouds – Part 1: Cirrus types, Atmospheric Chemistry and Physics, 16, 3463–3483, https://doi.org/10.5194/acp-16-3463-2016, 2016.

Kuebbeler, M., Lohmann, U., Hendricks, J., and Kärcher, B.: Dust ice nuclei effects on cirrus clouds, Atmospheric Chemistry and Physics, 14, 3027–3046, https://doi.org/10.5194/acp-14-3027-2014, 2014.

Kärcher, B. and Lohmann, U.: A parameterization of cirrus cloud formation: Homogeneous freezing of supercooled aerosols, Journal of Geophysical Research: Atmospheres, 107, AAC 4–1–AAC 4–10, https://doi.org/10.1029/2001JD000470, 2002.

Kärcher, B. and Podglajen, A.: A Stochastic Representation of Temperature Fluctuations Induced by Mesoscale Gravity Waves, Journal of Geophysical Research: Atmospheres, 124, 11 506–11 529, https://doi.org/10.1029/2019JD030680, 2019.

Kärcher, B., Jensen, E. J., and Lohmann, U.: The Impact of Mesoscale Gravity Waves on Homogeneous Ice Nucleation in Cirrus Clouds, Geophysical Research Letters, 46, 5556–5565, https://doi.org/10.1029/2019GL082437, 2019.

Kärcher, B., DeMott, P. J., Jensen, E. J., and Harrington, J. Y.: Studies on the Competition Between Homogeneous and Heterogeneous Ice Nucleation in Cirrus Formation, Journal of Geophysical Research: Atmospheres, 127, e2021JD035 805, https://doi.org/10.1029/2021JD035805, e2021JD035805 2021JD035805, 2022.

Kärcher, B., Jensen, E. J., Pokrifka, G. F., and Harrington, J. Y.: Ice Supersaturation Variability in Cirrus Clouds: Role of Vertical Wind Speeds and Deposition Coefficients, Journal of Geophysical Research: Atmospheres, 128, e2023JD039 324, https://doi.org/10.1029/2023JD039324, e2023JD039324 2023JD039324, 2023.

Lohmann, U., Lüönd, F., and Mahrt, F.: An Introduction to Clouds: From the Microscale to Climate, Cambridge University Press, https://doi.org/10.1017/CBO9781139087513, 2016.

Maturilli, M., Holdridge, D. J., Dahlke, S., Graeser, J., Sommerfeld, A., Jaiser, R., Deckelmann, H., and Schulz, A.: Initial radiosonde data from 2019-10 to 2020-09 during project MOSAiC, https://doi.org/10.1594/PANGAEA.928656, 2021.

Maturilli, M., Sommer, M., Holdridge, D. J., Dahlke, S., Graeser, J., Sommerfeld, A., Jaiser, R., Deckelmann, H., and Schulz, A.: MOSAiC radiosonde data (level 3) [dataset publication series], https://doi.org/10.1594/PANGAEA.943870, 2022.

Murray, B. J., Wilson, T. W., Dobbie, S., and Cui, Z.: Heterogeneous nucleation of ice particles on glassy aerosols under cirrus conditions, Nature Geoscience, 3, 233–237, https://doi.org/10.1038/ngeo817, 2010.

Nixdorf, U., Dethloff, K., Rex, M., Shupe, M., Sommerfeld, A., Perovich, D., Nicolaus, M., Heuze´, C., Rabe, B., Loose, B., Damm, E., Gradinger, R., Fong., A, Maslowski, W., Rinke, A., Kwok, R., Spreen, G., Wendisch, M., Herber, A., Hirsekorn, M., Mohaupt, V., Frickenhaus, S., Immerz, A., Weiss-Tuider, K., König, B., Mengedoht, D., Regnery, J., Gerchow, P., Ransby, D., Krumpen, T., Morgenstern, A., Haas, C., Kanzow, T., Rack, F. R., Saitzev, V., Sokolov, V., Makarov, A., Schwarze, S., Wunderlich, T., Wurr, K., and Boetius, A.: MOSAiC extended acknowledgement, Zenodo, https://doi.org/10.5281/zenodo.5179738, 2021.

Ohneiser, K., Ansmann, A., Baars, H., Seifert, P., Barja, B., Jimenez, C., Radenz, M., Teisseire, A., Floutsi, A., Haarig, M., Foth, A., Chudnovsky, A., Engelmann, R., Zamorano, F., Bühl, J., and Wandinger, U.: Smoke of extreme Australian bushfires observed in the stratosphere over Punta Arenas, Chile, in January 2020: optical thickness, lidar ratios, and depolarization ratios at 355 and 532 nm, Atmospheric Chemistry and Physics, 20, 8003–8015, https://doi.org/10.5194/acp-20-8003-2020, 2020.

Ohneiser, K., Ansmann, A., Chudnovsky, A., Engelmann, R., Ritter, C., Veselovskii, I., Baars, H., Gebauer, H., Griesche, H., Radenz, M., Hofer, J., Althausen, D., Dahlke, S., and Maturilli, M.: The unexpected smoke layer in the High Arctic winter stratosphere during MOSAiC 2019–2020, Atmospheric Chemistry and Physics, 21, 15 783–15 808, https://doi.org/10.5194/acp-21-15783-2021, 2021.

Ohneiser, K., Ansmann, A., Kaifler, B., Chudnovsky, A., Barja, B., Knopf, D. A., Kaifler, N., Baars, H., Seifert, P., Villanueva, D., Jimenez, C., Radenz, M., Engelmann, R., Veselovskii, I., and Zamorano, F.: Australian wildfire smoke in the stratosphere: the decay phase in 2020/21 and impact on ozone depletion, Atmospheric Chemistry and Physics Discussions, 2022, 1–41, https://doi.org/10.5194/acp-2021-1097, 2022.

Podglajen, A., Hertzog, A., Plougonven, R., and Legras, B.: Lagrangian temperature and vertical velocity fluctuations due to gravity waves in the lower stratosphere, Geophysical Research Letters, 43, 3543–3553, https://doi.org/10.1002/2016GL068148, 2016.

Polly(2024): PollyNET lidar data base, available at: http://polly.tropos.de/, last access: 10 January, 2024.

Radenz, M., Bühl, J., Seifert, P., Baars, H., Engelmann, R., Barja González, B., Mamouri, R.-E., Zamorano, F., and Ansmann, A.: Hemispheric contrasts in ice formation in stratiform mixed-phase clouds: disentangling the role of aerosol and dynamics with ground-based remote sensing, Atmospheric Chemistry and Physics, 21, 17 969–17 994, https://doi.org/10.5194/acp-21-17969-2021, 2021.

Riechers, B., Wittbracht, F., Hütten, A., and Koop, T.: The homogeneous ice nucleation rate of water droplets produced in a microfluidic device and the role of temperature uncertainty, Phys. Chem. Chem. Phys., 15, 5873–5887, https://doi.org/10.1039/C3CP42437E, 2013.

Rigg, Y. J., Alpert, P. A., and Knopf, D. A.: Immersion freezing of water and aqueous ammonium sulfate droplets initiated by humic-like substances as a function of water activity, Atmospheric Chemistry and Physics, 13, 6603–6622, https://doi.org/10.5194/acp-13-6603-2013, 2013.

Schneider, J., Höhler, K., Wagner, R., Saathoff, H., Schnaiter, M., Schorr, T., Steinke, I., Benz, S., Baumgartner, M., Rolf, C., Krämer, M., Leisner, T., and Möhler, O.: High homogeneous freezing onsets of sulfuric acid aerosol at cirrus temperatures, Atmospheric Chemistry and Physics, 21, 14 403–14 425, https://doi.org/10.5194/acp-21-14403-2021, 2021.

Schröder, F., Kärcher, B., Fiebig, M., and Petzold, A.: Aerosol states in the free troposphere at northern midlatitudes, Journal of Geophysical Research: Atmospheres, 107, LAC 8–1–LAC 8–8, https://doi.org/10.1029/2000JD000194, 2002.

Shupe, M. D., Rex, M., Blomquist, B., Ola, P., Persson, G., Schmale, J., Uttal, T., Althausen, D., Angot, H., Archer, S., Bariteau, L., Beck, I., Bilberry, J., Bucci, S., Buck, C., Boyer, M., Brasseur, Z., Brooks, I. M., Calmer, R., Cassano, J., Castro, V., Chu, D., Costa, D., Cox, C. J., Creamean, J., Crewell, S., Dahlke, S., Damm, E., de Boer, G., Deckelmann, H., Dethloff, K., Dütsch, M., Ebell, K., Ehrlich, A., Ellis, J., Engelmann, R., Fong, A. A., Frey, M. M., Gallagher, M. R., Ganzeveld, L., Gradinger, R., Graeser, J., Greenamyer, V., Griesche, H., Griffiths, S., Hamilton, J., Heinemann, G., Helmig, D., Herber, A., Heuzé, C., Hofer, J., Houchens, T., Howard, D., Inoue, J., Jacobi, H.-W., Jaiser, R., Jokinen, T., Jourdan, O., Jozef, G., King, W., Kirchgaessner, A., Klingebiel, M., Krassovski, M., Krumpen, T., Lampert, A., Landing, W., Laurila, T., Lawrence, D., Lonardi, M., Loose, B., Lüpkes, C., Maahn, M., Macke, A., Maslowski, W., Marsay, C., Maturilli, M., Mech, M., Morris, S., Moser, M., Nicolaus, M., Ortega, P., Osborn, J., Pätzold, F., Perovich, D. K., Petäjä, T., Pilz, C., Pirazzini, R., Posman, K., Powers, H., Pratt, K. A., Preußer, A., Quéléver, L., Radenz, M., Rabe, B., Rinke, A., Sachs, T., Schulz, A., Siebert, H., Silva, T., Solomon, A., Sommerfeld, A., Spreen, G., Stephens, M., Stohl, A., Svensson, G., Uin, J., Viegas, J., Voigt, C., von der Gathen, P., Wehner, B., Welker, J. M., Wendisch, M., Werner, M., Xie, Z., and Yue, F.: Overview of the MOSAiC expedition: Atmosphere, Elementa: Science of the Anthropocene, 10, https://doi.org/10.1525/elementa.2021.00060, 2022.

Skrotzki, J., Connolly, P., Schnaiter, M., Saathoff, H., Möhler, O., Wagner, R., Niemand, M., Ebert, V., and Leisner, T.: The accommodation coefficient of water molecules on ice – cirrus cloud studies at the AIDA simulation chamber, Atmospheric Chemistry and Physics, 13, 4451–4466, https://doi.org/10.5194/acp-13-4451-2013, 2013.

Spichtinger, P. and Cziczo, D. J.: Impact of heterogeneous ice nuclei on homogeneous freezing events in cirrus clouds, Journal of Geophysical Research: Atmospheres, 115, https://doi.org/https://doi.org/10.1029/2009JD012168, 2010.

Spichtinger, P. and Gierens, K. M.: Modelling of cirrus clouds – Part 1a: Model description and validation, Atmospheric Chemistry and Physics, 9, 685–706, https://doi.org/10.5194/acp-9-685-2009, 2009.

Spichtinger, P., Gierens, K., and Dörnbrack, A.: Formation of ice supersaturation by mesoscale gravity waves, Atmospheric Chemistry and Physics, 5, 1243–1255, https://doi.org/10.5194/acp-5-1243-2005, 2005.

Spichtinger, P., Marschalik, P., and Baumgartner, M.: Impact of formulations of the homogeneous nucleation rate on ice nucleation events in cirrus, Atmospheric Chemistry and Physics, 23, 2035–2060, https://doi.org/10.5194/acp-23-2035-2023, 2023.

Wang, B. and Knopf, D. A.: Heterogeneous ice nucleation on particles composed of humic-like substances impacted by O_3, Journal of Geophysical Research: Atmospheres, 116, https://doi.org/10.1029/2010JD014964, 2011.

Wang, B., Lambe, A. T., Massoli, P., Onasch, T. B., Davidovits, P., Worsnop, D. R., and Knopf, D. A.: The deposition ice nucleation and immersion freezing potential of amorphous secondary organic aerosol: Pathways for ice and mixed-phase cloud formation, Journal of Geophysical Research: Atmospheres, 117, https://doi.org/https://doi.org/10.1029/2012JD018063, 2012.

Westbrook, C. D., Hogan, R. J., and Illingworth, A. J.: The Capacitance of Pristine Ice Crystals and Aggregate Snowflakes, Journal of the Atmospheric Sciences, 65, 206 – 219, https://doi.org/10.1175/2007JAS2315.1, 2008.

Wolf, M., Zhang, Y., Zawadowicz, M., Goodell, M., Froyd, K., Freney, E., Sellegri, K., Rösch, M., Cui, T., Winter, M., Lacher, L., Axisa, D., Axisa, D., DeMott, P. J., Levin, E., T., J., Gute, E., Abbatt, J., Koss, A., Kroll, J. H., Surratt, J. D., and Cziczo, D. J.: A biogenic secondary organic aerosol source of cirrus ice nucleating particles, Nature Communications, 11, https://doi.org/10.1038/s41467-020-18424-6, 2020.